

Simulating hadronic physics on noisy intermediate-scale quantum devices using basis light-front quantization

Michael Kreshchuk ¹, Shaoyang Jia ^{2,3}, William M. Kirby ¹, Gary Goldstein,¹ James P. Vary ² and Peter J. Love^{1,4}

¹*Department of Physics and Astronomy, Tufts University, Medford, Massachusetts 02155, USA*

²*Department of Physics and Astronomy, Iowa State University, Ames, Iowa 50011, USA*

³*Physics Division, Argonne National Laboratory, Argonne, Illinois 60439, USA*

⁴*Computational Science Initiative, Brookhaven National Laboratory, Upton, New York 11973, USA*



(Received 30 November 2020; revised 7 April 2021; accepted 26 April 2021; published 3 June 2021)

The analogy between quantum chemistry and light-front quantum field theory, first noted by Wilson, serves as motivation to develop light-front quantum simulation of quantum field theory. We demonstrate how calculations of hadron structure can be performed on noisy intermediate-scale quantum devices within the basis light-front quantization (BLFQ) framework. Within BLFQ, relativistic quantum field theories take a form that permits direct application of methods for digital quantum simulation of quantum chemistry, which can be readily scaled into the quantum advantage regime. We calculate the light-front wave functions of pions using an effective light-front Hamiltonian in a basis representation on a current quantum processor. We use the variational quantum eigensolver to find the ground-state energy and the corresponding wave function, which is subsequently used to calculate pion mass radius, decay constant, elastic form factor, and charge radius.

DOI: [10.1103/PhysRevA.103.062601](https://doi.org/10.1103/PhysRevA.103.062601)

I. INTRODUCTION

In [1], Feynman was first to suggest that general quantum systems could only be efficiently simulated by machines obeying quantum laws themselves. The best-known classical algorithms for simulating multiparticle systems arising in quantum chemistry and solid-state physics already require resources growing exponentially with either the problem size or the numerical precision. Simulation of quantum field theory raises the complexity bar even further, owing to the formally infinite number of degrees of freedom per unit volume [2].

Quantum simulation has long been proposed as a promising application of quantum computing [3–9]. In the past five years there has been substantial progress both in optimal algorithms for large-scale quantum computers [10–14], and in hybrid quantum-classical algorithms suitable for noisy intermediate-scale quantum (NISQ) computers [15–18].

Quantum simulation of quantum field theory (QFT) has experienced a recent surge of interest, since Jordan, Lee, and Preskill proposed the first digital quantum algorithms for simulation of QFT [2,19,20]. Approaches based on analog quantum simulations using trapped ions [21] and cold atoms have been well established [22–26]. There also exist proposals for simulation of QFT using continuous variable quantum systems [27,28], as well as a large number of works using NISQ devices [29–35].

Widely explored techniques, based on the lattice discretization [2,36–38], were shown to be asymptotically efficient.

However, these proposals require qubit counts several orders of magnitude larger than those estimated in the large-scale architectural studies of Shor’s algorithm [39,40]. Consequently, new methods in simulating QFT with a practical number of qubits are merited.

In our previous work [41] we demonstrated that the light-front (LF) quantization of quantum field theory provides a natural framework for *ab initio* digital quantum simulation of QFT in the second-quantized formulation. In this paper, we continue our program of investigating quantum simulation in the light-front (LF) formulation [42] by developing an approach to simulating field theory based on the basis light-front quantization (BLFQ) [43,44] technique. The basis-function expansion allows us to further reduce the need for computational resources estimated in [41] making calculations accessible for existing quantum devices.

In [41] we developed quantum algorithms based on simulating time evolution and adiabatic state preparation in the discretized light-cone quantization (DLCQ) formalism. In the current work, we instead aim for near-term devices by adopting the variational quantum eigensolver (VQE) paradigm [15]: This allows us to implement a demonstration on the IBM Vigo quantum processor. VQE is a hybrid quantum-classical algorithm. The classical computer minimizes the expectation value of the Hamiltonian with respect to some parametrized Ansatz state, and the quantum computer is used only to repeatedly evaluate the expectation value. The resulting parametrized quantum circuit approximately prepares the ground-state wave function of the Hamiltonian. Thus, once the VQE procedure is complete, we can compute the expectation values of other observables in this approximate ground state.

The DLCQ and BLFQ paradigms provide alternative approaches to describing relativistic interactions. While both

Published by the American Physical Society under the terms of the Creative Commons Attribution 4.0 International license. Further distribution of this work must maintain attribution to the author(s) and the published article’s title, journal citation, and DOI.

are, in principle, *ab initio* frameworks, DLCQ studies the system starting from the light-front Hamiltonian quantized in the traditional free-field basis placed on a discrete momentum grid. BLFQ starts from the same light-front Hamiltonian but quantizes it in terms of modes tailored to the symmetries of the system under consideration in order to construct a computationally efficient representation of the Hamiltonian. Since each represents a choice of basis spaces for the fields, they should yield the same results in fully converged calculations, i.e., in their respective continuum limits.

Having much in common with *ab initio* methods in both quantum chemistry and nuclear theory the BLFQ formulation provides an ideal framework for benchmarking NISQ devices and testing existing algorithms on physically relevant problems such as the calculation of hadronic spectra [45–48] and parton distribution functions (PDFs) [49–51]. In essence, BLFQ amounts to (1) choosing the effective field theory most efficiently describing the problem of interest, (2) quantizing the system in the light-cone coordinates, (3) nonperturbatively solving the theory in the most suitable basis. This results in an efficient representation of the QFT problem under study. One typically starts with a fixed-particle-number formulation, effectively reducing the QFT setting to a quantum-mechanical many-body problem. In many cases, already at this level one can obtain results with suitable precision to make meaningful comparisons with experimental results [46–52]. An alternative approach, which also bears much in common with quantum chemistry, based on conformal truncation was proposed in [35].

In this article, we consider the dynamics of light mesons, which are described as relativistic strongly-interacting systems of quarks and gluons. We therefore encounter an infinite number of degrees of freedom in the corresponding QFT, whose treatment, upon truncation, requires classical resources exponential in cutoffs. However, being able to increase cutoffs is crucial to approach the continuum limit. We suggest an efficient approach (i.e., polynomial in all input parameters) for this problem, based on the synthesis of BLFQ and VQE paradigms.

While the computational methods we develop apply to simulations of multiparticle systems, in order to match the capabilities of existing devices and demonstrate the efficiency of the BLFQ formulation, we illustrate our approach by considering the dynamics of valence quarks for light mesons on the light front using the Hamiltonian from [52]. This Hamiltonian includes the kinetic energy, the confinement potential in both the longitudinal and the transverse directions [46], and the Nambu–Jona-Lasinio (NJL) interaction [53] to account for the chiral interactions among quarks. The dependence of the light-front wave functions for these valence quarks on the relative momentum is expanded in terms of orthonormal basis functions. After implementing finite cutoffs in this expansion, the light-front Hamiltonian becomes a Hermitian matrix in this basis representation. We use the same scheme as in Ref. [52] to fix our model parameters at each choice of basis cutoffs. To find the lowest eigenvalue of this BLFQ Hamiltonian, the pion mass squared, we run the VQE minimization on the IBM Vigo machine. Using the resulting wave function, we subsequently calculate decay constant, mass radius, electromagnetic form factor, and charge radius of the pion.

The two different *Ansätze* we consider in this paper are based on different ways of encoding physical states on the quantum computer. Within the *direct encoding* one stores the occupancies of the second-quantized states in the unary form and uses the unitary coupled cluster *Ansatz* for state preparation. Within a more efficient *compact encoding*, one stores the occupancies in the binary form, which requires logarithmically fewer qubits and allows one to prepare an *Ansatz* state using algorithms for arbitrary state preparation [54,55], given that the particle number is fixed and small.

While no quantum simulations on NISQ machines to date exceed the capabilities of classical computers, these are small examples of problems that rapidly grow out of reach for classical computers as more degrees of freedom are included [43]. As quantum resources grow, we will be able to expand the Hilbert space to include the dynamical gluons of QCD which are necessary to fully describe strong-interaction phenomena. With that basis expansion, we will be able to improve the treatment of chiral symmetry breaking provided by the phenomenological NJL model. An initial demonstration of BLFQ applied to heavy mesons, including a dynamical gluon, without the NJL model, also presents a successful nonperturbative renormalization method [56].

In Sec. II, we provide a summary of the BLFQ formalism and a representation of basis functions, which we used throughout the paper. In Sec. III, we derive expressions for various observables in the chosen basis. In Sec. IV we describe two variations of the VQE algorithm, and show the results of running it on an existing quantum computer.

II. BASIS LIGHT-FRONT QUANTIZATION

A. Overview

The light-front quantization approach specifies the commutation relation of fields at equal light-front time [57]. In contrast to the Lagrangian formulation of equal-time quantization, the field-theory dynamics after light-front quantization is governed by a light-front Hamiltonian [57] responsible for the light-front time evolution of the system. Quantizing a QFT on the light front has the following advantages: Triviality of the vacuum, absence of ghost fields in the light-cone gauge, Hamiltonian sparsity, and the simple form of observables in terms of the wave functions. Within this Hamiltonian approach, the bound-state masses and associated wave functions are solvable from the light-front time-independent Schrödinger equation.

In [41] we developed a simulation algorithm based on the DLCQ, allowing one to achieve optimal scaling with the DLCQ parameters for *ab initio* quantum simulation of QFT. In this work, we bring the computational requirements into the range of the capabilities of existing quantum devices. We achieve this by efficiently representing the Hamiltonian in the framework of BLFQ [43,44].

Within BLFQ, a field is expanded in terms of second-quantized Fock states representing occupancies of modes (first-quantized basis functions), and there is no *a priori* limit on the number of the degrees of freedom [43,58]. Accordingly, our algorithms are designed to efficiently simulate QFT applications where particle number needs not to be conserved.

TABLE I. Flow of growing complexity and computational resources (left to right) for quantum simulation of quantum field theory on the light front. Basis light-front quantization (BLFQ) may be considered to encapsulate discrete light-cone quantization (DLCQ). However, we use the distinct terms here to emphasize that classical preprocessing is used in BLFQ with minimal bases for the purpose of obtaining approximations using relatively few quantum resources. The goal is to accelerate convergence to the continuum limit for bound-state observables and, hence, to optimally use existing quantum resources in the NISQ era for these problems. Treatment of open systems, such as resonances and strong decays, will likely require DLCQ to be implemented on future fault-tolerant quantum computers.

Regime	VQE			Fault-tolerant
	Two-body sector BLFQ, relative coordinate basis	Valence sector BLFQ, single- coordinate basis	Multiparticle BLFQ, single- coordinate basis	Multiparticle DLCQ, single- coordinate basis
Encoding	Compact	Compact or direct		Compact
State preparation	Arbitrary state preparation	Arbitrary state preparation or unitary coupled cluster or QITE		Adiabatic state preparation
Measurement	Pauli	Pauli or sparse		Sparse

However, for QFTs at low resolution, BLFQ is often restricted to the valence degrees of freedom. This allows us to simulate it on an existing quantum chip. These experiments represent the first stage shown in Table I, which illustrates a progression of methods that scale towards fault-tolerant simulation of QFTs in the quantum supremacy regime. Notice that the methods we propose in this article apply to the first three stages in Table I. The final stage was discussed in [41].

Previous development of BLFQ for the heavy mesons is partially based on the holographic confinement potential between the valence quark and antiquark in the holographic transverse directions [46–48]. This potential is supplemented by a longitudinal confinement potential to attain a three-dimensional spherical confinement potential in the non-relativistic limit. These potentials are constructed independent of the spins for the quark and the antiquark and they are governed by a single overall strength parameter. In addition to the kinetic energy and the confinement potentials, they form the baseline Hamiltonian that is analytically solvable and defines our basis functions [46,52]. These basis functions possess desired spatial symmetries and boost invariances. The derived effective one-gluon exchange interaction based on the gauge dynamics serves as the spin-orbit interaction and incorporates a running coupling [46].

In this article we adopt the Hamiltonian in Ref. [52] for the light mesons. Specifically, the same confinement potential forms as those in Ref. [46] are implemented. However, we do not include the one-gluon exchange because the interactions for light quarks manifest from the chiral symmetry, which is insufficiently accounted for by a perturbative expansion of the gauge interaction. Instead, we resort to the Nambu–Jona-Lasinio (NJL) model for the chiral interaction of these quarks [53,59,60]. Within our basis representation, the matrix elements of the NJL interaction can be calculated analytically [52]. We compute the lowest mass eigenvalue and its corresponding eigenvector, its light-front wave function, using the algorithm to be described in Sec. IV. We then calculate observables based on this eigenvector.

B. Effective Hamiltonian of the BLFQ-NJL model

The light-front wave functions (LFWFs) of the valence quarks for the π^+ meson and the K^+ meson have been solved

from Ref. [52] in the basis light-front quantization (BLFQ) framework using Nambu–Jona-Lasinio interactions [53,59–61] on a classical computer. Specifically, one first truncates the light-front wave function for the mesons to the valence quark Fock sector such that the state vector is expressed as

$$|\Psi(P^+, \vec{P}^\perp)\rangle = \sum_{r,s} \int_0^1 \frac{dx}{4\pi x(1-x)} \times \int \frac{d\vec{k}^\perp}{(2\pi)^2} \psi_{rs}(x, \vec{k}^\perp) b_r^\dagger(xP^+, \vec{k}^\perp + x\vec{P}^\perp) \times d_s^\dagger[(1-x)P^+, -\vec{k}^\perp + (1-x)\vec{P}^\perp]|0\rangle, \quad (1)$$

where $P = k + p$ is the total momentum of the meson, $x = k^+/P^+$ is the longitudinal momentum fraction carried by the valence quark, and $\vec{k}^\perp = \vec{k}^\perp - x\vec{P}^\perp$ is the relative transverse momentum.

In order to solve for the LFWFs for the valence quarks inside light mesons, we adopt the effective Hamiltonian that can be represented as a basis-diagonal term and the NJL interaction:

$$H_{\text{eff}} = H_0 + H_{\text{int}}^{\text{eff}}. \quad (2)$$

The basis-diagonal term H_0 contains the kinetic energy of the valence quarks, the transverse confinement potential, and the longitudinal confinement potential. In the valence Fock sector of mesons, this term takes the form of

$$H_0 = \frac{(\vec{k}^\perp)^2 + \mathbf{m}^2}{x} + \frac{(\vec{k}^\perp)^2 + \bar{\mathbf{m}}^2}{1-x} + b^4 x(1-x) \vec{r}_\perp^2 - \frac{b^4}{(\mathbf{m} + \bar{\mathbf{m}})^2} \partial_x x(1-x) \partial_x, \quad (3)$$

where x is the longitudinal momentum fraction carried by the valence quark and \vec{k}_\perp is the relative transverse momentum of the valence quarks. The masses of the valence quark and the valence antiquark are given by \mathbf{m} and $\bar{\mathbf{m}}$, respectively. In addition, b specifies the strength of the confinement potentials. This part of the Hamiltonian has analytic solutions that constitute the basis states for the BLFQ approach as will be seen in detail in Sec. II C.

When quarks in the confinement region are the only retained degrees of freedom, the strong interaction among them

can be understood to arise from the global chiral symmetry, an approximate symmetry of quantum chromodynamics. To model this chiral interaction, we employ the interaction in the scalar-pseudoscalar channel of the color-singlet NJL model [53]. Specifically, we ignore both the instantaneous interaction and the self-energy correction from the NJL interaction to obtain the following term in the total Hamiltonian:

$$H_{\text{int}}^{\text{eff}} = H_{\text{NJL},\pi}^{\text{eff}} = \int dx^- \int d\vec{x}^\perp \left(-\frac{G_\pi P^+}{2} \right) \times [(\bar{\psi}\psi)^2 + (\bar{\psi}i\gamma_5\vec{\tau}\psi)^2]. \quad (4)$$

Here ψ is the fermion field operator, G_π is the NJL coupling constant, and P^+ is the total light-front longitudinal momentum of the system. We then expand Eq. (4) into relevant combinations of ladder operators for the quark fields. In the basis representation, this term further takes the form of a Hermitian matrix, the elements of which can be calculated analytically [52].

In this work, we solve the eigenvalue problem defined by Eq. (2) in the total angular momentum $J_z = 0$ block with the lowest eigenstates of H_0 forming the longitudinal and radial basis states for the interacting Hamiltonian.

In this representation, the effective Hamiltonian takes the form of a 4×4 matrix indexed by the basis quantum number θ that specifies the angular and spin excitations. The explicit expressions for elements in this matrix are given in Appendix A 2.

C. Basis-function representations of wave functions for valence quarks of mesons

We adopt the following expansion of the light-front wave function for the valence quarks given by Eq. (1):

$$\psi_{rs}(x, \vec{k}^\perp) = \sum_{nml} \psi_{nmrs} \phi_{nm} \left(\frac{\vec{k}^\perp}{\sqrt{x(1-x)}}; b \right) \chi_l(x), \quad (5)$$

where ψ_{nmrs} is the expansion coefficient, ϕ_{nm} is a two-dimensional (2D) harmonic oscillator (HO) eigenfunction, and χ_l is the longitudinal basis function. Here r and s are the spin indices of the quark and the antiquark, respectively. Each term in Eq. (5) is an eigenfunction of H_0 in Eq. (3). Explicitly, ϕ_{nm} is defined as

$$\phi_{nm}(\vec{q}^\perp; b) = \frac{1}{b} \sqrt{\frac{4\pi n!}{(n+|m|)!}} \left(\frac{|\vec{q}^\perp|}{b} \right)^{|m|} \times \exp\left(-\frac{\vec{q}^{\perp 2}}{2b^2}\right) L_n^{|m|} \left(\frac{\vec{q}^{\perp 2}}{b^2} \right) e^{im\varphi}, \quad (6)$$

with $\tan(\varphi) = q^2/q^1$ and $L_n^{|m|}$ being the associated Laguerre function. The parameter b sets the scale of the harmonic oscillator eigenfunction, which we choose to be identical to the confining strength in the light-front Hamiltonian. Meanwhile,

$\chi_l(x)$ is given by

$$\chi_l(x; \alpha, \beta) = \sqrt{4\pi(2l + \alpha + \beta + 1)} \times \sqrt{\frac{\Gamma(l+1)\Gamma(l + \alpha + \beta + 1)}{\Gamma(l + \alpha + 1)\Gamma(l + \beta + 1)}} \times x^{\beta/2} (1-x)^{\alpha/2} P_l^{(\alpha, \beta)}(2x-1), \quad (7)$$

with $P_l^{(\alpha, \beta)}(z)$ being the Jacobi polynomial and

$$\alpha = 2\bar{\mathbf{m}}(\mathbf{m} + \bar{\mathbf{m}})/\kappa^2, \quad (8a)$$

$$\beta = 2\mathbf{m}(\mathbf{m} + \bar{\mathbf{m}})/\kappa^2. \quad (8b)$$

When we solve the eigenvalue problem defined by the BLFQ-NJL Hamiltonian, the following cutoffs on the basis quantum numbers following Ref. [52] are imposed:

$$0 \leq n \leq N_{\text{max}}, \quad -M_{\text{max}} \leq m \leq M_{\text{max}}, \quad 0 \leq l \leq L_{\text{max}}. \quad (9)$$

Sensitivity of observable results to basis cutoffs in BLFQ has been explored in, for example, [62].

Because truncations on different basis quantum numbers are independent, we call this truncation scheme the orthogonal enumeration. Such a scheme allows us to solve simultaneously for eigenstates with different azimuthal angular momentum projection J_z , since it is a good quantum number in this basis. The size of the Hamiltonian in the basis representation with this orthogonal enumeration is $n_{\text{H}} \times n_{\text{H}}$, with

$$n_{\text{H}} = 4(N_{\text{max}} + 1)(2M_{\text{max}} + 1)(L_{\text{max}} + 1). \quad (10)$$

However, the capacity of NISQ devices motivates further reduction in the dimension of the Hilbert space spanned by our basis representation. Specifically, because eigenfunctions of this Hamiltonian have fixed azimuthal angular momentum projection J_z , the basis quantum number θ indexes specific combinations of the spin and orbital bases in the orthogonal enumeration as specified in Appendix A 1. Each basis state in the fixed J_z block is then given by the basis quantum numbers n, l , and θ . In the limit of $M_{\text{max}} = 2$, the unitary transformation that relates the bases in the fixed J_z blocks to those in the orthogonal enumeration is given by Table VI. The degeneracy in the basis quantum number θ in each J_z block is apparent in Table VI. For example, when $J_z = 0$, this degeneracy is $d_\theta = 4$. With a given set of (n, l, θ) in a given J_z block, we take the convention such that the index of this basis is given by

$$a(n, l, \theta) = [n(L_{\text{max}} + 1) + l]d_\theta + \theta. \quad (11)$$

For a given index, the corresponding basis quantum numbers can be easily calculated. Consequently, the size of the Hamiltonian for a fixed J_z in this new enumeration becomes

$$n_{\text{H}0} = d_\theta(N_{\text{max}} + 1)(L_{\text{max}} + 1), \quad (12)$$

which is smaller than n_{H} given by Eq. (10). This provides an example of how one may exploit the symmetries embedded in the chosen BLFQ Hamiltonian to achieve gains in computational efficiency.

III. COMPUTING OBSERVABLES FROM THE VALENCE LFWF

One of the many advantages of the light-front approach to quantum field theories is that observables for bound states can be easily extracted from light-front wave functions. Explicitly, measurement operators corresponding to physical observables usually take a simple form, resulting in efficient measurements on a quantum computer (see Sec. IV and Appendix D). In this section, we demonstrate how to calculate the decay constant, mass radius, valence parton distribution function, and elastic form factor.

A. Decay constant

The meson decay constants are defined as the matrix elements of current operators between the vacuum and the meson wave functions [46]. They correspond to amplitudes of the wave functions at the coordinate-space origin. Specifically, the decay constants for scalar mesons (f_S), pseudoscalar mesons (f_P), vector mesons (f_V), and axial vector mesons (f_A) are defined as

$$\langle 0 | \bar{\psi} \gamma^\mu \psi | S(p) \rangle = p^\mu f_S, \quad (13a)$$

$$\langle 0 | \bar{\psi} \gamma^\mu \gamma_5 \psi | P(p) \rangle = i p^\mu f_P, \quad (13b)$$

$$\langle 0 | \bar{\psi} \gamma^\mu \psi | V(p) \rangle = \epsilon_\lambda^\mu(p) m_V f_V, \quad (13c)$$

$$\langle 0 | \bar{\psi} \gamma^\mu \gamma_5 \psi | A(p) \rangle = \epsilon_\lambda^\mu(p) m_A f_A, \quad (13d)$$

respectively. Here the polarization vector for the vector mesons is defined as

$$\epsilon_\lambda^\mu(p) = \begin{cases} \left(\frac{p^+}{m_{V,A}}, \frac{\vec{p}^{\perp 2} - m_{V,A}^2}{m_{V,A} p^+}, \frac{\vec{p}^\perp}{m_{V,A}} \right) & \text{for } \lambda = 0, \\ \left(0, \frac{2\vec{e}_\lambda^\perp \cdot \vec{p}^\perp}{p^+}, \vec{e}_\lambda^\perp \right) & \text{for } \lambda = \pm 1 \end{cases} \quad (14)$$

with $\vec{e}_\pm^\perp = (1, \pm i)/\sqrt{2}$.

In terms of the valence-sector light-front wave functions, expressions for these decay constants are reduced into [46]

$$f_{P,A} = 2\sqrt{N_c} \int_0^1 \frac{dx}{4\pi\sqrt{x(1-x)}} \int \frac{d^2\kappa^\perp}{(2\pi)^2} \times [\psi_{+-}(x, \vec{\kappa}^\perp) - \psi_{-+}(x, \vec{\kappa}^\perp)] \Big|_{m_J=0}, \quad (15a)$$

$$f_{S,V} = 2\sqrt{N_c} \int_0^1 \frac{dx}{4\pi\sqrt{x(1-x)}} \int \frac{d^2\kappa^\perp}{(2\pi)^2} \times [\psi_{+-}(x, \vec{\kappa}^\perp) + \psi_{-+}(x, \vec{\kappa}^\perp)] \Big|_{m_J=0}, \quad (15b)$$

with the condition $m_J = m + s_1 + s_2 = 0$ specifying that only the states with zero angular momentum projections are used in the calculation. Here $N_c = 3$ is the number of colors.

In our basis representation, the integrals over the longitudinal momentum fraction and the relative transverse momenta in Eq. (15) can be evaluated exactly. Details of this calculation can be found in Appendix B 1. Since the decay constant is linear in the wave function, we only need to calculate these

integrals for each basis function. Subsequently, the decay constants in the basis representation are given by

$$f_{P,A} = 2\sqrt{\frac{N_c}{\pi}} \sum_{n,l} (-1)^n L_l(1/2, 1/2; \alpha, \beta) \times (\psi_{n0l+-} - \psi_{n0l-+})|_{m_J=0}, \quad (16)$$

$$f_{S,V} = 2\sqrt{\frac{N_c}{\pi}} \sum_{n,l} (-1)^n L_l(1/2, 1/2; \alpha, \beta) \times (\psi_{n0l+-} + \psi_{n0l-+})|_{m_J=0}, \quad (17)$$

where the longitudinal integrals $L_l(a, b; \alpha, \beta)$ are defined and given analytically in Appendix B 3. Because the overall phase of the LFWF remains undetermined by the Hamiltonian, only the absolute value of the decay constant carries physical significance. Once the LFWF $|\psi\rangle$ in our basis representation is known on a quantum computer, the calculation of the corresponding decay constant can be thought of as computing $|\langle v | \psi \rangle|$ for some fixed $|v\rangle$.

B. Mass radius

The mass radius is the square root of the expectation value for the relative transverse separation of the valence quarks. It can be calculated from the valence two-body wave function based on Eq. (33) of Ref. [46]. Specifically for the pseudoscalar mesons, we have

$$\langle r_m^2 \rangle = \frac{3}{2} \sum_{r,s} \int_0^1 \frac{dx}{4\pi} \int d\vec{r}^\perp x(1-x)\vec{r}^{\perp 2} \times \tilde{\psi}_{rs}^*(x, \vec{r}^\perp) \tilde{\psi}_{rs}(x, \vec{r}^\perp), \quad (18)$$

where $\tilde{\psi}_{rs}(x, \vec{r}^\perp)$ is the light-front wave function depending on the longitudinal momentum fraction x and the relative transverse coordinate \vec{r}^\perp . It is related to the momentum-space wave function by the Fourier transform in the transverse momenta $\vec{\kappa}^\perp$. Explicitly, we have

$$\tilde{\psi}_{rs}(x, \vec{r}^\perp) = \sqrt{x(1-x)} \sum_{nml} \psi_{nm lrs} \tilde{\phi}_{nm}(\sqrt{x(1-x)}\vec{r}^\perp) \chi_l(x), \quad (19)$$

with

$$\tilde{\phi}_{nm}(\vec{r}^\perp) = b \sqrt{\frac{n!}{(n+|m|)! \pi}} (b|\vec{r}^\perp|)^{|m|} \times \exp\left[-\frac{b^2 \vec{r}^{\perp 2}}{2}\right] L_n^{|m|}(b^2 \vec{r}^{\perp 2}) \times \exp[i m \phi_r + i(n+|m|/2)\pi], \quad (20)$$

and $\tan \phi_r = r_2/r_1$.

To calculate the mass radius in terms of expansion coefficients $\psi_{nm l s_1 s_2}$, we first need to evaluate the following

dimensionless integrals of the basis functions:

$$\begin{aligned}
I_m(n', m', l'; n, m, l) & \\
&\equiv \int_0^1 dx \chi_{l'}(x) \chi_l(x) \\
&\times \int_0^{+\infty} d|\vec{r}^\perp|^2 \int_0^{2\pi} \frac{d\phi_r}{8\pi} x^2 (1-x)^2 b^2 |\vec{r}^\perp|^2 \\
&\times \tilde{\phi}_{n',m'}^*(\sqrt{x(1-x)}\vec{r}^\perp) \tilde{\phi}_{n,m}(\sqrt{x(1-x)}\vec{r}^\perp). \quad (21)
\end{aligned}$$

We then have the square of the radius given by

$$\langle r_m^2 \rangle = \frac{3}{2b^2} \sum_{rs} \sum_{n'm'l'nml} \psi_{n'm'l'rs}^* I_m(n', m', l'; n, m, l) \psi_{nmlrs}. \quad (22)$$

The explicit expression for the matrix $I_m(n', m', l'; n, m, l)$ is available in Appendix B 2, which takes the form of a Hermitian matrix in our basis representation.

C. Parton distribution function of valence quarks

The probability of finding a quark inside a meson carrying momentum fraction x is given by

$$\begin{aligned}
f(x) &= \frac{1}{4\pi x(1-x)} \\
&\times \sum_{rs} \int \frac{d\vec{k}^\perp}{(2\pi)^2} \psi_{rs}^*(x, \vec{k}^\perp) \psi_{rs}(x, \vec{k}^\perp) \\
&= \frac{1}{4\pi} \sum_{n,m,l',l,r,s} \psi_{nml'rs}^* \psi_{nmlrs} \chi_{l'}(x) \chi_l(x), \quad (23)
\end{aligned}$$

which is interpreted as the PDF for the valence quark. The PDF for the valence antiquark is given by $f(1-x)$ [49–51]. We use the solutions of ψ_{nmlrs} defined in Eq. (5) to calculate the valence PDFs of mesons.

Notice that Eq. (23) defines a bilinear of the light-front wave functions in the basis representation. To compute the PDF with the LFWFs obtained from a quantum computer, let us rewrite Eq. (23) as

$$f(x) = \frac{1}{4\pi} \sum_{l',l} \rho_{l',l} \chi_{l'}(x) \chi_l(x), \quad (24a)$$

$$\rho_{l',l} = \sum_{n,m,r,s} \psi_{nml'rs}^* \psi_{nmlrs}. \quad (24b)$$

Elements of the density matrix $\rho_{l',l}$ defined in Eq. (24b) can be evaluated as the expectation value of the corresponding projection operators on a quantum computer, and subsequently used to calculate the PDF in Eq. (24a).

D. Elastic form factor for pseudoscalar mesons

To calculate the elastic form factors from the light-front wave functions within the impulse approximation where the photon interacts with the meson through the quark-photon vertex, we apply the following formula [63,64] within the

Drell-Yan frame $P'^+ = P^+$:

$$\begin{aligned}
I_{m'_j, m_j}(Q^2) &= \frac{1}{2P^+} \langle \Psi(P', m'_j) | \\
&\times \sum_f e_f \bar{\psi}_f(0) \gamma^+ \psi_f(0) | \Psi(P, m_j) \rangle \\
&= \sum_{rs} \int \frac{dx}{4\pi x(1-x)} \int \frac{d^2 k^\perp}{(2\pi)^2} \\
&\times \{ e_q \psi_{rs}^{*m'_j}(x, \vec{k}^\perp + (1-x)\vec{q}^\perp) \\
&- e_{\bar{q}} \psi_{rs}^{*m'_j}(x, \vec{k}^\perp - x\vec{q}^\perp) \} \psi_{rs}^{m_j}(x, \vec{k}^\perp), \quad (25)
\end{aligned}$$

with $q = P' - P$ and $Q^2 = -q^2$. The operator inside the Dirac bracket is the charge density operator on the light front, with e_f being the charge carried by the quark of flavor f in units of the elementary charge and the summation running over all quark flavors. Additionally, e_q is the charge of the quark ($e_u = +\frac{2}{3}$ for an up quark). While $e_{\bar{q}}$ is the charge of the antiquark ($e_{\bar{d}} = -\frac{1}{3}$ for an anti-down quark). Detailed derivation of Eq. (25) is given in Appendix C 1.

In the basis representation, we apply the Talmi-Moshinsky transform to simplify the integrals in the transverse momentum, leaving the longitudinal integral to be evaluated numerically for each Q^2 . Following steps in Appendix C 2, we rewrite the electromagnetic form factors into a bilinear form of the valence wave function:

$$\begin{aligned}
I_{m'_j, m_j}(Q^2) &= \sum_{n'm'l'} \sum_{n,m,l} \sum_{r,s} \psi_{n'm'l'rs}^* \\
&\times \tilde{C}(n', m', l'; n, m, l; Q^2) \psi_{nmlrs}. \quad (26)
\end{aligned}$$

The operator \tilde{C} is defined according to Eq. (C19). At a given Q^2 , the form factor can be calculated using the LFWFs obtained from a quantum computer by taking the expectation value of the Hermitian operator $\tilde{C}(n', m', l'; n, m, l; Q^2)$.

Specifically, the elastic form factors of the pseudoscalar mesons are given by

$$F_P(Q^2) = I_{0,0}(Q^2). \quad (27)$$

The charge radius is then specified by the first Taylor expansion coefficient of the elastic form factor at the origin:

$$\langle r_c^2 \rangle = -6 \lim_{Q^2 \rightarrow 0} \frac{d}{dQ^2} F_P(Q^2). \quad (28)$$

IV. QUANTUM-COMPUTATIONAL METHODS

The approach to quantum simulation of Hamiltonian dynamics of QFTs taken in [65] is as follows: (a) initialize the system in a certain state of the free Hamiltonian, (b) adiabatically turn on the interaction, (c) if necessary, evolve the system with time, and (d) measure the energy (or another observable) of the system using the phase estimation algorithm [3,8,65]. While measurements in certain cases may have simpler form [37,41], the state preparation still constitutes a major challenge not viable for near-term devices due to limits in qubit numbers and in gate fidelities. This motivates the variational quantum eigensolver (VQE), an approach to finding Hamiltonian eigenvalues in which a NISQ device is used as a part of a hybrid quantum-classical

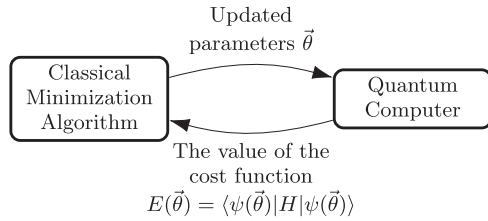


FIG. 1. Schematic of the variational quantum eigensolver (VQE). The parameter vector $\vec{\theta}$ completely specifies the *Ansatz* wave function.

algorithm [15,32,34,66,67]. In VQE, a quantum computer prepares a given variational state and evaluates the Hamiltonian expectation value, which a classical computer performs a gradient search to minimize (see Fig. 1). To prepare the variational state, we adopt an *Ansatz* specified by parameters $\vec{\theta}$, which are controlled by the classical minimization.

While in [41] we focused on *ab initio* simulations which are likely to become available in the fault-tolerant regime, in this paper we investigate the use of NISQ devices for high-energy nuclear physics calculations on the light front. Therefore, unlike in [41], we formulate the problem as a VQE instance.

We begin by briefly reviewing the VQE method. For the VQE algorithm, as with classical variational algorithms, to be efficient and accurate, it is essential to come up with a parametrized *Ansatz* state $|\psi(\vec{\theta})\rangle$ that is easy to prepare and is expected to have significant overlap with the true ground state. In addition, the *Ansatz* should be based significantly on the structure of the Hamiltonian under consideration. *Ansatz* states that do not include problem structure can suffer from barren plateaus that prevent convergence of the optimization [68–70]. Even for structured *Ansatz* states, sufficient noise may cause a noise-induced barren plateau to occur, again frustrating the optimization [71]. In this case, one can use other state preparation methods such as quantum imaginary-time evolution [72,73]. Below we shall consider different choices of *Ansatz* state preparation procedures, encodings of the physical states in a quantum computer, and classical optimization algorithms.

While using VQE for simulating a Hamiltonian problem, the major steps are as follows:

(1) Define the state and operator mapping, i.e., a correspondence between the physical states and the multiqubit states of a quantum computer, as well as the mapping between the operators acting on these spaces.

(2) Choose a parametrized *Ansatz* state. One typically writes the *Ansatz* state as

$$|\psi(\vec{\theta})\rangle = U(\vec{\theta})|\psi_0\rangle, \quad (29)$$

where $|\psi_0\rangle$ is a fixed reference state, and $U(\vec{\theta})$ is the VQE *Ansatz* operator.

One possibility is to choose the form of $U(\vec{\theta})$ to resemble the form of the Hamiltonian evolution operator [66].

(3) Once the state $|\psi(\vec{\theta})\rangle$ is prepared for a given set of parameters $\vec{\theta}$, one evaluates the cost function by measuring

the expectation value of the multiqubit Hamiltonian operator:

$$E(\vec{\theta}) = \langle \psi(\vec{\theta}) | \hat{H} | \psi(\vec{\theta}) \rangle. \quad (30)$$

The algorithm can only be considered efficient if the number of measurements grows polynomially with the problem complexity (discussed further below).

(4) The value of the cost function is then sent to the classical optimizer, which either determines the set of parameters for the next iteration of the algorithm, or terminates the algorithm if the desired precision has been achieved.

We shall explore two approaches to simulating problems in the BLFQ formulation, based on two different encoding schemes. The first of these is the *direct encoding*, widely used in quantum chemistry [8,74]. In such an encoding scheme, one assigns a particular set of qubit registers to each physical (basis) degree of freedom. In application to purely fermionic systems, one may use one qubit to encode one fermionic second-quantized mode, which leads one to the Jordan-Wigner (JW) encoding [75]. Thus, one needs N qubits in order to encode N fermionic modes. The fermionic raising and lowering operators are represented by N -local multiqubit operators, due to the need to enforce anticommutation relations. One can alternatively employ the Bravyi-Kitaev (BK) encoding [76–79] that uses N qubits to store N fermionic modes, with operators being only $\log N$ local. Circuits implementing VQE *Ansatz* operators are typically based on Trotterization [66].

The second encoding we employ is *compact encoding*, as was explored in [41] for front-form physics, and also in the context of quantum chemistry in [8]. The idea is to only store the occupied modes of multiparticle Fock states. With this encoding, future quantum computers will be able to simulate time evolution using sparsity-based techniques that are optimal in all parameters [11–13,41,80,81]. In our example, we use arbitrary state preparation as a VQE *Ansatz*.

A. Direct encoding

In order to run a simulation on a current quantum device, in this work we consider a scenario where the particle number is fixed. However, since quantum advantage is likely to be achieved only in the multiparticle regime, it is essential to keep our methods extendable to this general regime.

A natural way of formulating a multiparticle problem is by using the second-quantized formalism. Consider a Hamiltonian of the form

$$\hat{H} = \hat{H}_1 + \hat{H}_2 + \dots, \quad (31)$$

where

$$\hat{H}_1 = \sum_{i,j} h_{ij} a_i^\dagger a_j, \quad \hat{H}_2 = \sum_{i,j,k,l} h_{ijkl} a_i^\dagger a_j^\dagger a_k a_l. \quad (32)$$

Here h_{ij} represents the single-body interactions, while h_{ijkl} and higher-order terms correspond to many-body interactions. For the first experimental implementation, we restrict ourselves to $\hat{H} = \hat{H}_1$ (with h_{ij} being the meson valence sector BLFQ Hamiltonian matrix), for two reasons. First, owing to the efficiency of the BLFQ formulation, considering the single-body part of the Hamiltonian is oftentimes enough to yield reasonable results [45,49,51,52,62]. Second, keeping the

TABLE II. The multiqubit representation of the four physical one-particle states in the direct and compact encodings.

Basis state index	Direct encoding	Compact encoding
1	0001⟩	00⟩
2	0010⟩	01⟩
3	0100⟩	10⟩
4	1000⟩	11⟩

particle number fixed is suitable for benchmarking, paralleling state-of-the-art experimental results in quantum simulation of chemistry [82].

In the light-front formulation, the gauge degrees of freedom are treated on equal footing with those of matter fields, by restricting to the *light-cone gauge* and adding the corresponding second-quantized interaction terms to the Hamiltonian [43,57,83–86]. Methods we propose below extend naturally to this scenario [87–89], using known encodings of bosonic modes and creation and annihilation operators [88,90–92].

Within the JW encoding, the multiqubit states $|\dots f_2 f_1 f_0\rangle$ mimic the second-quantized fermionic states: The qubit f_i stores the occupancy of the $(i+1)$ th orbital (see Table II). In order to enforce anticommutation relations, the fermionic creation and annihilation operators are represented by N -local multiqubit operators [75]. We shall use this encoding for the rest of the section; simulation in the Bravyi-Kitaev encoding is discussed in Appendix E.

Since one typically solves the problem in a basis found by means of some classical approximation, the reference state $|\psi_0\rangle$ can be chosen to have a simple form in terms of basis vectors; in the simplest case, it may coincide with one of the basis vectors. Next, we would like to design an *Ansatz* operator that acts on the reference state to prepare an *Ansatz* state that ideally has large overlap with the exact ground state. An example of such an operator is the unitary coupled cluster (UCC) [66]. Choosing the form of the *Ansatz* operator to resemble the form of the Hamiltonian ensures that one can explore the regions of the Hilbert space that can be reached via the Hamiltonian evolution, and also guarantees that the symmetries are preserved. For the Hamiltonian of the form (32) one writes the UCC as [66]

$$U(\vec{\theta}) = e^{T-T^\dagger}, \quad T = T_1 + T_2 + \dots, \\ T_1 = \sum_{\substack{i \in \text{occ} \\ a \in \text{virt}}} \theta_a^i a_a^\dagger a_i, \quad T_2 = \sum_{\substack{i > j \in \text{occ} \\ a > b \in \text{virt}}} \theta_{ab}^{ij} a_a^\dagger a_b^\dagger a_i a_j, \quad (33)$$

where *occ* and *virt* denote occupied and unoccupied orbitals in the reference state $|\psi_0\rangle$. Physically, the action of the UCC operator allows one to transfer “some amplitude” from initially

occupied orbitals to the unoccupied ones. For real Hermitian Hamiltonians, the coefficients in (33) are real.

We would now like to translate (33), which was written in terms of the fermionic operators, into its qubit representation. According to the JW transformation [75], the qubit operators are obtained as

$$a_j^\dagger a_i - a_i^\dagger a_j \mapsto \frac{i}{2} Y_1 Z_2 \dots Z_{j-1} X_j - \frac{i}{2} X_1 Z_2 \dots Z_{j-1} Y_j, \quad (34)$$

where X_i, Y_i, Z_i are the Pauli matrices acting on qubit i . Substituting (34) into (33) generates a mapping

$$U(\vec{\theta}) \mapsto e^{i \sum_j \alpha_j P_j}, \quad (35)$$

where P_j are the Pauli operators, while α_j are the corresponding real coefficients. Trotterization of the expression above leads to

$$U(\vec{\theta}) \mapsto \left(\prod_j e^{i \frac{\alpha_j}{\rho} P_j} \right)^\rho, \quad (36)$$

where ρ is the Trotter number, which can be typically chosen quite small in VQE [93], in contrast with the case of simulating time evolution.

The traditional approach to calculating the expectation value as in (30) amounts to expanding the Hamiltonian in the basis of Pauli operators using (34):

$$\langle \psi(\vec{\theta}) | \hat{H} | \psi(\vec{\theta}) \rangle = \sum_i h_i \langle \psi(\vec{\theta}) | P_i | \psi(\vec{\theta}) \rangle. \quad (37)$$

The expectation values of individual Pauli terms on the right-hand side of (37) can be efficiently measured via sampling from the state $|\psi(\vec{\theta})\rangle$ [15].

The optimal parameters $\vec{\theta}^*$, obtained upon successful termination of the VQE algorithm, allow one to prepare the VQE approximation to the ground state of the system. By analogy with (37), this can be used to calculate the expectation value of any observable bilinear in the wave function [i.e., of the form $\langle \psi(\vec{\theta}) | \hat{O} | \psi(\vec{\theta}) \rangle$], such as mass radius, PDF, or elastic form factor. Observables linear in the wave function [i.e., of the form $\langle v | \psi(\vec{\theta}) \rangle$], where $|v\rangle$ is a constant vector], such as the decay constant in Eq. (15b), can be calculated using the simple circuit shown in Fig. 2.

Efficiency analysis

When proposing new algorithms for quantum simulations on NISQ devices, it is essential to elicit their scaling properties in order to distinguish aspects of a particular simulation that may lead to quantum advantage from those that couldn't. The question relevant to this paper is which aspects of the few-qubit calculations can we scale up to several hundred qubits. Concomitantly, we would like to elucidate which aspects of the few-qubit calculations are amenable to efficient classical calculations and which are not.

TABLE III. Model parameters for the BLFQ-NJL model.

$\mathbf{m}, \bar{\mathbf{m}}$	κ, b	G_π	N_{\max}	M_{\max}	L_{\max}
337.01 MeV	227.00 MeV	250.785 GeV ⁻²	0	2	0

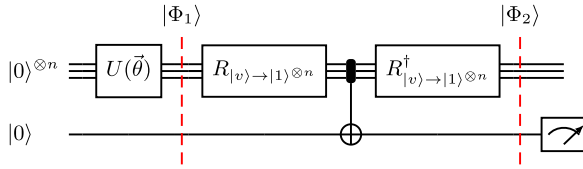


FIG. 2. Estimating the magnitude of the inner product $\langle v | \psi(\vec{\theta}) \rangle$ for fixed $|v\rangle$. Up to the first dashed line, the circuit prepares the VQE *Ansatz* state by applying the *Ansatz* circuit $U(\vec{\theta})$ to the first set of registers, resulting in the state $|\Phi_1\rangle = |\psi(\vec{\theta})\rangle \otimes |0\rangle$. The next rotation $R_{|v\rangle \rightarrow |1\rangle^{\otimes n}}$ represents any unitary operator that maps the state $|v\rangle$ to the state $|1\rangle^{\otimes n}$. Thus, the state $|\Phi_2\rangle$ at the second dashed line is given by $|\Phi_2\rangle = \langle v | \psi(\vec{\theta}) \rangle |1\rangle \otimes |1\rangle + (|\psi(\vec{\theta})\rangle - \langle v | \psi(\vec{\theta}) \rangle |v\rangle) \otimes |0\rangle$. The quantity $|\langle v | \psi(\vec{\theta}) \rangle| = \sqrt{|\langle v | \psi(\vec{\theta}) \rangle|^2}$ is found as the square root of the probability for the *ancilla* qubit to collapse into the state $|1\rangle$.

The stages of one shot of a VQE calculation are *Ansatz* preparation and measurement of all Hamiltonian terms. Many shots with fixed *Ansatz* parameters are required to obtain one estimate of the expectation value of the Hamiltonian. Many estimations of the expectation value of the Hamiltonian are required to optimize the *Ansatz* parameters. Typically, the resources required to optimize a given VQE *Ansatz* to a fixed precision cannot be bounded theoretically. This is what makes VQE a heuristic method. However we can determine the computational cost of each step in a single shot and ensure that the quantum gates and qubits required scale polynomially with the problem size.

As a prototypical example, consider the problem of finding a ground state in quantum chemistry using VQE. The parameters describing the complexity of the problem are the total number of orbitals N and the number of electrons in the system M (i.e., the number of occupied orbitals). Using the direct mapping requires N qubits for encoding physical states. The second-quantized Hamiltonian operator can be written as a polynomial in ladder operators. Those, in turn, are each represented by a polynomial number of Pauli operators, each of which is at most $\log N$ local. Therefore, the measurement of the Hamiltonian operator can be replaced with the measurement of a polynomial number of elementary operators. Each of those can be measured with precision ϵ using $O(\epsilon^{-2})$ samples [15,16].

All that remains is to quantify the operational resources for preparing the *Ansätze*. In quantum chemistry in the direct mapping, these are typically prepared using a unitary coupled cluster (UCC) operator. The UCC *Ansatz* operator including single and double excitations (UCCSD) contains $O(N^2 M^2)$ free parameters. Application of the (Trotterized) *Ansatz* operator to the initial state is realized by a circuit containing a polynomial number of gates since the action of fermionic ladder operators can be represented by a polynomial number of gates in the case of direct encoding.

Let us now see how these arguments can be naturally extended to the case of quantum field theory (QFT). First of all, we note that unlike in quantum chemistry, where the number of particles is conserved, QFT allows for processes of creation and annihilation of particles. Nevertheless, light-front QFT does have an operator similar to the nonrelativistic number operator, namely, the total momentum operator. Indeed,

since this relativistic momentum operator commutes with the Hamiltonian, one can solve the problem within a Fock space sector of a fixed total momentum.

This analogy extends to the terms in the Hamiltonian. In quantum chemistry, the Hamiltonian operator can be written as a polynomial of fermionic creation and annihilation operators, containing $O(\text{poly}(N))$ terms. In QFT, the second-quantized Hamiltonian operator can be written as a polynomial of ladder operators, containing $O(\text{poly}(\Lambda))$ terms, where Λ is the momentum cutoff. As in chemistry, in the direct encoding those can be represented by $\log \Lambda$ local Pauli operators, whose total number consequently also scales as $O(\text{poly}(\Lambda))$. To obtain a finite-dimensional Hilbert space in the equal-time quantization, one would have to impose an additional cutoff on the number of excitations in each bosonic mode. However, in the LF formalism the maximum number of excitations is automatically limited by *harmonic resolution* K , the dimensionless light-cone momentum [41,57]. Within the BLFQ, the role of Λ and K is played by N_{\max} , M_{\max} , and L_{\max} cutoffs (introduced in Sec. II C). Therefore, all the resources for a single VQE estimation of the QFT Hamiltonian expectation value based on the direct encoding and UCC will grow polynomially in momentum cutoffs and precision. Consider as an example a Hamiltonian of the form (31), with both single- and two-body interaction terms included. Simulating a system with N modes would require measuring $O(N^3)$ Pauli operators [94,95] and considering circuits with $O(N^4)$ gates [[66], Sec. II A].

B. Compact encoding

In our previous work [41] we explored the possibility of using the compact encoding for simulating physics on the light front. This amounts to only storing information about occupied modes in the Fock states. In the simplified setting considered in Sec. II B, due to the usage of relative coordinates, the only information we store is the index of the single occupied orbital. While in the direct mapping the index of the occupied orbital was stored in the unary form, requiring N qubits for N orbitals, in the compact mapping it is stored in the binary form, requiring $\lceil \log_2 N \rceil$ qubits for N orbitals. Therefore, in the case when the single-body Hamiltonian matrix h_{ij} is of size $N \times N = 2^n \times 2^n$, one would use all the basis states of the 2^n -dimensional Hilbert space of n qubits (see Table II).

In the compact mapping, an equation analogous to (34) would contain an exponential number of terms on the right-hand side, thus making the usage of the UCC inefficient. Instead, one may employ any of existing arbitrary state preparation algorithms [54,55]. While their complexity is exponential in the number of qubits, in our case the number of qubits is itself logarithmic in the problem cutoffs.

For the direct encoding, in order to measure the expectation value of the Hamiltonian we can express the Hamiltonian in terms of Pauli operators. Any observable of size $N \times N = 2^n \times 2^n$ can be expanded in the basis of $4^n = N^2$ Pauli operators defined on n qubits:

$$h = \sum_{\alpha=1}^{N^2} c_{\alpha} P_{\alpha}, \quad c_{\alpha} = \frac{1}{2^n} \text{tr}(h P_{\alpha}), \quad (38)$$

where c_{α} are *real*.

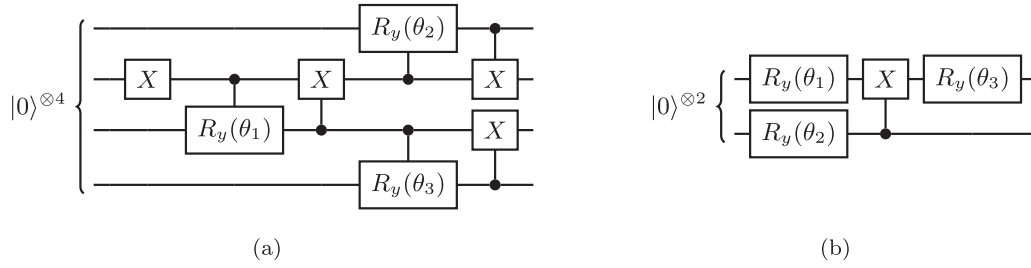


FIG. 3. *Ansatz* circuits for preparing an arbitrary superposition of single-particle Fock states with real coefficients. For the direct encoding (a), we use a generalization of a circuit from [55] for preparation of W_N states. For the binary encoding (b), we use arbitrary state preparation, with all single-qubit rotations replaced by $R_y(\theta)$ gates, where $R_y(\theta)$ denotes a single-qubit rotation through an angle θ about the y axis. After transpiling into native QISKIT gates, the circuits look as in Fig. 4.

It should be emphasized that the logarithmic scaling of the number of qubits required as a function of the problem cutoffs implies that the Hilbert space dimension is polynomial in the cutoffs. This also implies that classical approaches to this problem are efficient. We are considering these specific initial problems as benchmarks, where the results obtained can be compared to the known classical solution as an evaluation of the NISQ device itself.

Efficiency analysis

Within the VQE regime, the approach to quantum simulation based on the compact mapping is more efficient than the one based on the direct encoding when solving a two-body problem in the relative variable basis. As one starts to consider the problem in the multiparticle setting, the number of qubits required for storing physical states in the compact encoding is nearly optimal [41]. Despite that, one faces serious problems at the stages of state preparation and measurement. Since the complexity of arbitrary state preparation algorithms scales exponentially with the number of qubits, and the number of qubits grows linearly with the number of occupied modes, those algorithms can only be used if the number of particles is fixed and small. Of course, in principle, one could use sparsity-based techniques for state preparation, but this produces gate counts that are not feasible in the NISQ era. Therefore, coming up with a good *Ansatz* for a multiparticle state in the compact encoding is an important task, which we leave for future work.

Another problem arises at the measurement stage: The number of Pauli terms in the expansion of the Hamiltonian grows exponentially with the number of qubits. However, the

Hamiltonian matrix in the basis of Fock states is sparse because it contains polynomially many creation and annihilation operator monomials and each of these connects a Fock state to at most one other Fock state. Therefore, we can use the formulation of VQE for sparse Hamiltonians described in [96] for the multiparticle compact encoding case.

V. RESULTS

In this section we describe numerical and experimental results of implementing VQE for a sample QFT problem, namely, simulation of a pion in the minimal BLFQ representation. In order to run our simulation on an existing device, we shall use the 4×4 light meson BLFQ Hamiltonian from Sec. II B corresponding to $J_z = 0$ sector in Table VI (see also Appendix A 2), with the choice of model parameters specified in Table III.

$$H^{\text{BLFQ}} = \begin{pmatrix} 640323 & 139872 & -139872 & -107450 \\ 139872 & 346707 & 174794 & 139872 \\ -139872 & 174794 & 346707 & -139872 \\ -107450 & 139872 & -139872 & 640323 \end{pmatrix}, \tag{39}$$

in units of MeV^2 . In the notations of equation (32), we assume that operators a_i^\dagger create two-particle states of the form (1), and set $h_{ij} = H^{\text{BLFQ}}$ and $h_{ijkl} = 0$ (see also the discussion in [42]). The two lowest eigenvalues correspond to π and ρ meson squared masses: The ground state is $(0.34, -0.62, -0.62, 0.34)^T$, with $m_\pi^2 = 139.6^2 \text{ MeV}^2$.

We can analyze the VQE calculation in a few steps: (a) Check that the classical optimizer is working correctly. To



FIG. 4. QISKIT circuits for (a) preparing a superposition of single-occupancy states with real amplitudes, (b) preparing a two-qubit state with real amplitudes. Circuits before transpiling are shown in Fig. 3.

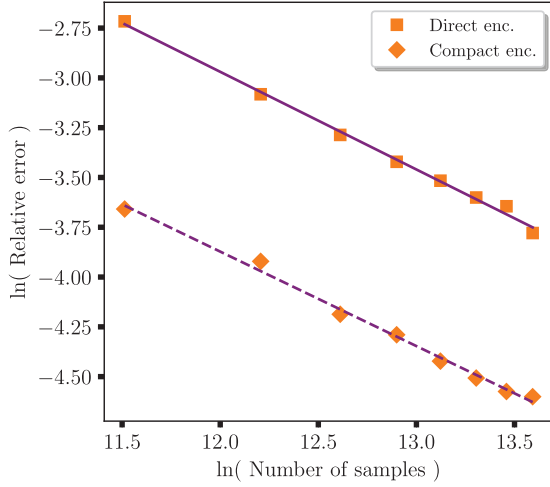


FIG. 5. Precision vs number of samples for ground-state energy obtained via sampling from the exact distribution. Fitting gives $n \approx 382/\epsilon^{2.04}$ (direct encoding) and $n \approx 46/\epsilon^{2.1}$ in (compact encoding), confirming the theoretical $n \sim O(1/\epsilon^2)$ dependence. Compact encoding shows better convergence due to having shorter circuits on fewer qubits [compare Figs. 3(a) and 3(b)].

eliminate any errors arising due to sampling, we begin with evaluating the Hamiltonian expectation values exactly, using the state vector representation. (b) Determine the number of steps required to reach the desired precision when evaluating the expectation value via sampling from the exact distribution. This gives the lower bound on the number of samples, and models the situation of using a “perfect quantum computer.” (c) Evaluate expectation values on the IBM Vigo quantum processor. (d) Use error mitigation techniques to postprocess the results obtained on the quantum computer. We shall perform these steps using both the direct and compact encodings, evaluating the Hamiltonian eigenstate as well as other observables discussed in Sec. III.

The multiqubit states representing the four physical basis states are shown in Table II. The states in the direct encod-

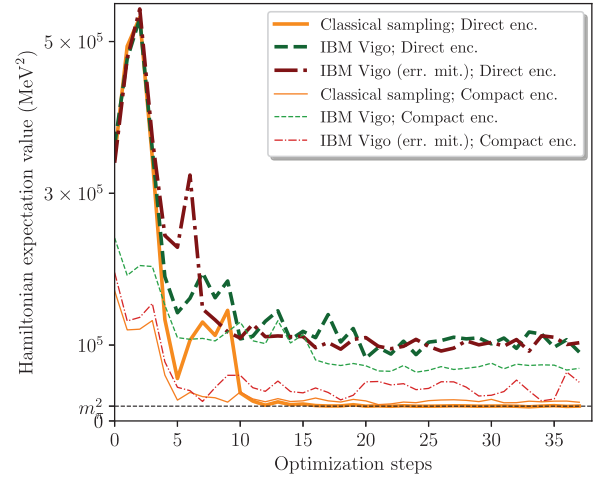


FIG. 6. The results of the VQE minimization algorithm in the compact and direct encodings. These were obtained from 8192 samples per term on IBM Vigo machine, with and without measurement error mitigation. The results for the case when the expectation values are evaluated using the state vector are not shown; they reach the exact result after ~ 15 steps.

ing can be thought of as JW-encoded states. Therefore, we use the JW transformation for calculating the corresponding multiqubit Hamiltonian:

$$\begin{aligned}
 H_{\text{direct}}^{\text{BLFQ}} &= 987031IIII + 87397(IXXI + IYYI) \\
 &\quad - 53725(YZZY + XZZX) - 320161(IIIZ + ZIII) \\
 &\quad - 173353(IZII + IIZI) + 69936(IIYY + IIXX \\
 &\quad + YZYI + XZXI - IYZY - IXZX - YYII - XXII),
 \end{aligned} \tag{40}$$

where each term is a tensor product of single-qubit Pauli matrices I, X, Y, Z . (In what follows, we use this convention

TABLE IV. Expectation values of various observables calculated in the ground state obtained by means of the VQE minimization. The observables are pion mass squared (m_π^2), mass radius squared ($\langle r_m \rangle^2$), and decay constant squared (f_π^2). These were obtained from 8192 samples per term on IBM Vigo chip, with and without measurement error mitigation. Classical sampling means sampling from the exact probability distribution. Observables are shown both including constant terms (the physically relevant values), and not including them (the measured values). In the case of m_π^2 , the physically relevant observable is obtained as a result of a massive cancellation between a large positive constant term and a large negative experimentally measured quantity [see Eqs. (40) and (41) and the first two rows of the table]. The fractional errors for observables are shown in Fig. 7. The parameters of the model are chosen so that for minimal choice of cutoffs, adopted in this sample calculation, the pion mass squared would match its experimental value.

	Direct encoding				Compact encoding			
	Exact	Classical sampling	IBM Vigo	IBM Vigo, err. mit.	Exact	Classical sampling	IBM Vigo	IBM Vigo, err. mit.
m_π^2 , MeV ² , no constant	-967550	-969199	-888630	-889465	-474034	-477417	-428465	-437639
m_π^2 , MeV ²	19481	17832	98401	97567	19481	16099	65051	55876
$\langle r_m \rangle^2$, fm ² , no constant	-2.52	-2.51	-2.39	-2.39	-0.56	-0.56	-0.46	-0.55
$\langle r_m \rangle^2$, fm ²	1.39	1.40	1.52	1.52	1.39	1.40	1.49	1.41
f_π^2 , MeV ² , no constant	1027	1019	485	501	1975	1988	1589	1895
f_π , MeV	54.1	54.0	48.8	49.0	54.1	54.2	50.4	53.3

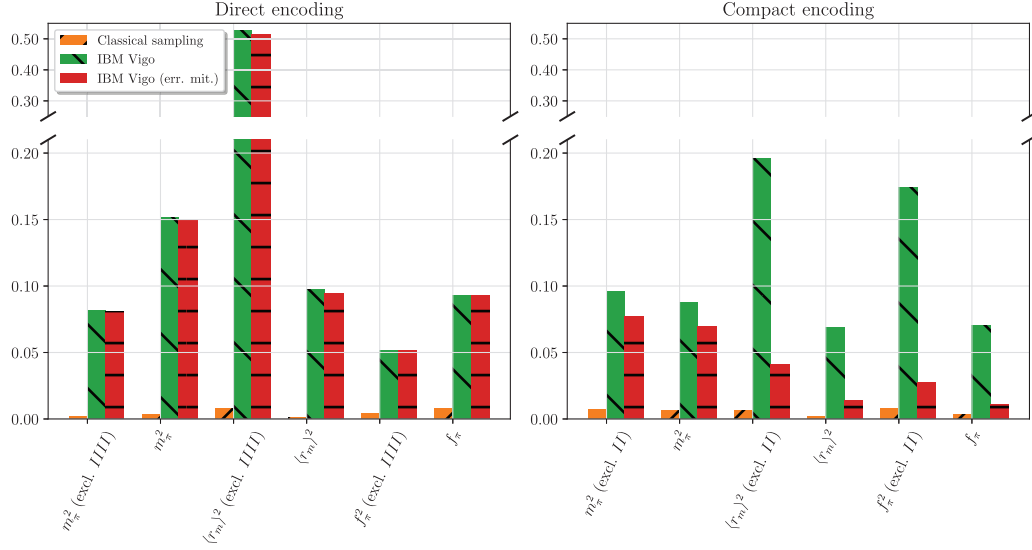


FIG. 7. Relative errors in estimates of various observables. These were obtained from 8192 samples per term on IBM Vigo machine, with and without measurement error mitigation. Physically significant observables have a significant contribution from the constant term in their multiqubit representation. Observables are shown with and without the contribution of the constant term. For the GS energy, the error was calculated relative to the second lowest eigenvalue m_p^2 . For the compact encoding, measurement error mitigation consistently improves the results.

when expanding Hermitian matrices in Pauli terms acting on qubits.)

As an *Ansatz* operator, one could use the UCCS (no doubles) operator. According to (33), T_1 will contain N terms, each of which is N local in the JW encoding and $\log N$ local in the BK encoding. In the former case, the circuit will contain $O(N^2)$ gates, while in the latter only $O(N \log N)$ gates. However, in order to further improve the gate count in the direct encoding-based algorithm, instead of the UCCS *Ansatz*, we design a simple parametrized circuit of depth $O(\log N)$ using $O(N)$ gates shown in Fig. 3(a), which is capable of

preparing an arbitrary superposition (with real amplitudes) of single-occupied states in the JW encoding. (This circuit is a generalization of the circuit proposed in [55] for preparing W_N states). Upon transpiling into native QISKIT [97] gates, the circuit shown in Fig. 3(a) looks as shown in Fig. 4(a). The multiqubit representation of the Hamiltonian in the compact encoding is obtained from (39), calculating the coefficients by applying (38):

$$H_{\text{compact}}^{\text{BLFQ}} = 493515II + 139872(ZX - XZ) + 33671XX + 141122YY + 146807ZZ. \quad (41)$$

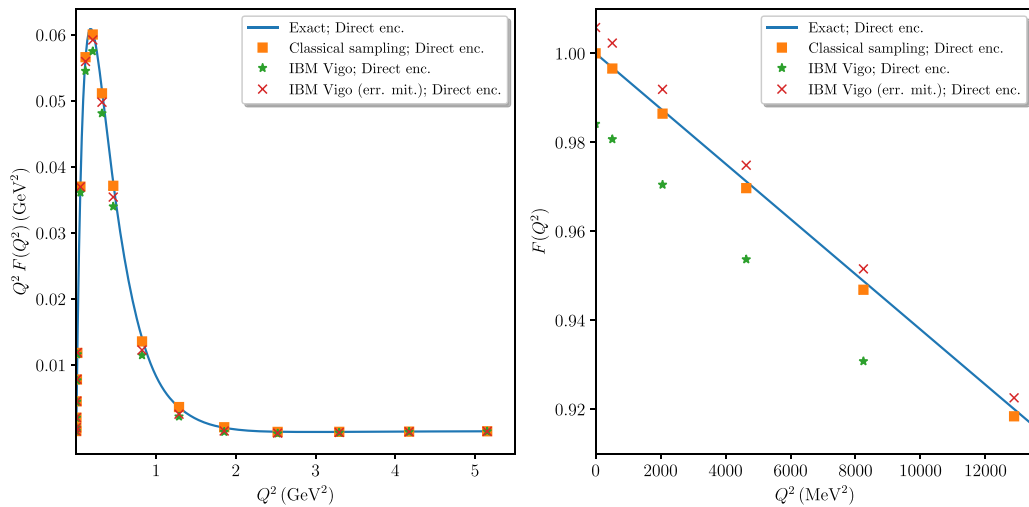


FIG. 8. Pion elastic form factor, as defined in Eq. (27). Pion elastic form factor is used to calculate the charge radius, obtaining the values given in Table V [charge radius is defined in Eq. (28)]. Data points for the quantum simulation on the IBM Vigo processor used 8192 samples per term, with and without measurement error mitigation. The results measured on the quantum computer are in good agreement with the exact ones due to the strong contribution to the measurement operators from the identity term. The results for the compact mapping are not shown as they are visually indistinguishable from the exact lines.

TABLE V. Pion charge radius, as defined in Eq. (28), calculated using the numerical results from Fig. 8.

Encoding	Charge radius $\sqrt{\langle r_c^2 \rangle}$, MeV ⁻¹	
	Direct	Compact
Exact	6.31×10^{-3}	6.31×10^{-3}
Classical sampling	6.29×10^{-3}	6.30×10^{-3}
IBM Vigo	6.33×10^{-3}	6.35×10^{-3}
IBM Vigo (err. mit.)	6.34×10^{-3}	6.31×10^{-3}

The *Ansatz* state is prepared using the circuit shown in Fig. 3(b), which prepares an arbitrary two-qubit state with real amplitudes. For both encodings, we need to estimate expectation values of Pauli operators. To do this, we first rotate to a basis in which the desired Pauli operator is diagonal, then measure single-qubit Z operators. The desired operator is a product of some set of single-qubit Z operators in this basis.

The classical optimization was performed using various algorithms from the `python.scipy.optimize` library. In agreement with [66], the best convergence to the true ground state was achieved with L-BFGS-B [98] and COBYLA [99] methods. The latter showed better convergence, and it is used in all the following calculations. Depending on the choice of the initial guess state, the optimizer was typically reaching four-digit precision after $\sim 10^1$ – 10^2 steps [for a good initial guess, such as $(0, -1/\sqrt{2}, 1/\sqrt{2}, 0)^T$] and up to a few hundred steps for randomly chosen initial state. In rare cases, the minimization was not converging. Next, we determined the number of samples from the exact distribution required to reach the desired precision, which is expected to scale as $O(1/\epsilon^2)$ [16]. To do so, we calculated the relative error for determining the Hamiltonian's expectation value in the true ground state using the classical simulation (the corresponding parameters of the circuits were obtained via the optimization at the previous stage). We performed 1000 experiments with a fixed number of samples, and calculated the root-mean square relative errors in determining the ground-state expectation value over each set of experiments. The results on Fig. 5 indicate that on an ideal quantum computer we would need to generate $\sim 10^6$ samples per Pauli term in order to reach 2% precision, and $\sim 4 \times 10^6$ samples to reach 1% precision.

In Fig. 6 we show the results of the VQE minimization procedure. Each Pauli term expectation value was estimated from 8192 samples on the IBM Vigo processor. At each minimization step we plot the resulting estimated energies, as well as those obtained by classical sampling from the exact probability distributions (the latter illustrates the performance of a noiseless quantum computer). The measurement error mitigation was performed with QISKIT's `CompleteMeasFitter`, which amounts to preparing and measuring all the 2^n possible n -qubit bitstrings (8192 shots each). These measurements allow one to define a calibration matrix of size $2^n \times 2^n$, which is later used for postprocessing counts. This error mitigation technique has cost exponential in the number of qubits and is not efficient. In the multiparticle setting, it has to be replaced with more complex noise models. The improvement due to measurement error mitigation was significant only for the compact encoding, and led to the best convergence to the

true ground-state energy out of all the experimental methods tested.

Table IV shows the expectation values for the energy, decay constant, and mass radius, evaluated in the approximate ground state obtained via the VQE minimization procedure, while Fig. 7 shows the relative errors. The expressions for all observables are obtained from the corresponding BLFQ matrices in analogy with Eqs. (40) and (41); the explicit expressions can be found in Appendix D. Note that all the observables have a dominant contribution from the unity term (*IIII* in the direct encoding and *II* in the compact encoding), whose expectation value is exactly 1. Therefore, in Fig. 7 we also show the expectation values for observables from which this term has been subtracted, which in certain cases improves the relative precision of results. The expectation values without the unit terms are the quantities actually measured on the quantum computer, while those including the unit terms are the physically relevant numbers, so the relative errors in both are of interest. In order to calculate the decay constant, one can use either the circuit shown in Fig. 2 or Pauli measurements; we use the latter option to minimize the number of gates.

The elastic form factors, Eq. (27), are shown in Fig. 8, and the corresponding charge radii, Eq. (28), are presented in Table V. In both cases, the results obtained on the quantum computer are in good agreement with the exact ones. This is to be expected because the corresponding measurement operators have a large contribution from the identity operator.

Results in Figs. 6–8 motivate further development of compact encoding simulation methods, such as those proposed in [96]. Another takeaway is that, as can be seen from Figs. 7

TABLE VI. The unitary transformation from the orthogonal enumeration to blocks with fixed J_z . The other basis quantum numbers n and l are identical in both representations. Here we only impose the basis cutoff of $M_{\max} = 2$, while cutoffs in l and n can be freely determined.

J_z	θ	m	s_1	s_2
-3	1	-2	-	-
-2	1	-2	+	-
-2	2	-2	-	+
-2	3	-1	-	-
-1	1	-2	+	+
-1	2	-1	+	-
-1	3	-1	-	+
-1	4	0	-	-
0	1	-1	+	+
0	2	0	+	-
0	3	0	-	+
0	4	1	-	-
1	1	0	+	+
1	2	1	+	-
1	3	1	-	+
1	4	2	-	-
2	1	1	+	+
2	2	2	+	-
2	3	2	-	+
3	1	2	+	+

and 8, relative errors for other observables can be comparable to or even smaller than those for the ground-state eigenvalue. Although our results are illustrative rather than general, they suggest that using VQE to study observables other than the Hamiltonian ground state alone will be fruitful in subsequent work.

With our choice of cutoffs, the calculation of PDFs in the compact encoding reduces to measurement of II , while in the direct encoding, it reduces to the projector onto the computational subspace (spanned by the single-occupancy Fock states). Thus, in both cases, the quantity to be measured on the quantum computer is trivial [i.e., $\rho_{0,0} = 1$, as in Eq. (23)], and the resulting PDF is $f(x) = \rho_{0,0} \chi_0^2(x) = 1 \times [2986 x^{4.4} (1-x)^{4.4}]^2$, because there is one single longitudinal mode due to choices in basis truncations.

VI. DISCUSSION

In this paper, we simulated high-energy nuclear physics in the light-front formulation on existing quantum processors. We considered a detailed example in which we studied a relativistic analog of hydrogen, the pion. We studied this problem in a fixed-particle-number formulation as a benchmarking test for existing devices, and as a preparation for moving towards the mixed-particle-number formulation. Using the basis light-front quantization (BLFQ) formalism, we demonstrated how small quantum computers can be used for calculating hadronic spectra and various structural observables. Adopting an effective interaction (suggested by the anti-de Sitter Space/quantum chromodynamics correspondence [100]) and

a set of basis functions (motivated by the particular problem of interest [43]) allows one to significantly reduce the computational resources, and to obtain reasonable results for realistic theories on devices having just a few qubits.

Within the VQE approach to quantum simulation, studied in this work, we considered various encodings and state preparation procedures, some of which were naturally suggested by our experience in quantum chemistry. Together with our previous paper [41], this work defines a spectrum of methods for quantum simulation of quantum field theories. On this spectrum, one can move from restricted models, to be simulated on existing quantum devices, all the way to full *ab initio* simulation of QCD in 3+1 dimensions [(3+1)D], to be simulated on future fault-tolerant quantum computers. Future work will expand and improve our methods on both ends of the spectrum. The next step in near-term simulation will be to switch to single-particle coordinates, providing the framework for mixed-particle-number simulations where quantum advantage is possible.

ACKNOWLEDGMENTS

W.M.K. acknowledges support from the National Science Foundation, Grant No. DGE-1842474. P.J.L., M.K., and G.G. acknowledge support from DOE HEP Grant No. DE-SC0019452. S.J. and J.P.V. acknowledge support from DOE Grants No. DE-FG02-87ER40371 and No. DE-SC0018223. S.J. also acknowledges support from DOE Office of Science, Office of Nuclear Physics, Contract No. DE-AC02-06CH11357.

APPENDIX A: HAMILTONIAN IN THE BASIS REPRESENTATION

1. Unitary transformation to the fixed J_z blocks

Because the light-front Hamiltonian conserves the angular momentum in the z direction, the Hamiltonian in our basis representation can be diagonalized into blocks of fixed J_z . This is equivalent to combining the spin quantum numbers s_1 and s_2 with the magnetic quantum number m to form a new quantum number θ . Specifically, when $M_{\max} = 2$, the unitary transformation from the original BLFQ basis to this block-diagonal form is given by Table VI.

2. BLFQ-NJL Hamiltonian in the $J_z = 0$ block

When $N_{\max} = L_{\max} = 0$, the light-front effective Hamiltonian in the $J_z = 0$ block takes the form of a 4×4 matrix H^{BLFQ} . The subscripts of the matrix then index the basis quantum number θ . The explicit expressions for these matrix elements are given in the following equations. Here κ is strength of the confining potential which we set identical to the basis scale b . The parameter G_π is the coupling constant of the NJL interaction. Functions $L'(a, b)$ and $L(a, b)$ both stand for $L_0(a, b; \alpha, \beta)$ given in Appendix B 3.

Explicitly, the matrix elements of this Hamiltonian in our basis representation are given by

$$H_{11}^{\text{BLFQ}} = (\mathbf{m} + \overline{\mathbf{m}})^2 + 5\kappa^2 + \frac{8G_\pi b^4}{\pi} L'(0, 0)L(0, 0), \quad (\text{A1a})$$

$$H_{12}^{\text{BLFQ}} = \frac{4G_\pi b^3}{\pi} \{\mathbf{m}\{[L'(0, 1)L(1/2, -1/2) - L'(0, 0)L(1/2, -1/2)] + \overline{\mathbf{m}}L'(0, 0)L(-1/2, 1/2)\}, \quad (\text{A1b})$$

$$H_{13}^{\text{BLFQ}} = -\frac{2G_\pi b^3}{\pi} L'(0, 0)\{\overline{\mathbf{m}}\{2L(-1/2, 1/2) + L(-1/2, 3/2) + L(1/2, 1/2)\} + 2\mathbf{m}L(1/2, -1/2)\}, \quad (\text{A1c})$$

$$H_{14}^{\text{BLFQ}} = -\frac{4G_\pi b^4}{\pi} \{L'(0, 1)L(1, 0) + L'(1, 0)L(0, 1) + L'(0, 1)L(0, 0) + L'(0, 0)L(0, 1) - 2L'(0, 1)L(0, 1) + 2L'(0, 0)L(0, 0)\}, \quad (\text{A1d})$$

$$H_{21}^{\text{BLFQ}} = H_{12}^{\text{BLFQ}}, \quad (\text{A1e})$$

$$\begin{aligned}
H_{22}^{\text{BLFQ}} = & (\mathbf{m} + \bar{\mathbf{m}})^2 + 3\kappa^2 - \frac{G_\pi b^2}{\pi} \bar{\mathbf{m}}\mathbf{m} \{L'(1/2, 1/2)L(-1/2, -1/2) + L'(-1/2, 1/2)L(1/2, -1/2) \\
& + L'(1/2, -1/2)L(-1/2, 1/2) + L'(-1/2, -1/2)L(1/2, 1/2) + L'(-1/2, 3/2)L(-1/2, -1/2) \\
& - 2L'(-1/2, 1/2)L(-1/2, 1/2) + L'(-1/2, -1/2)L(-1/2, 3/2)\} \\
& - \frac{2G_\pi b^2}{\pi} \{\bar{\mathbf{m}}L'(-1/2, 1/2) + \mathbf{m}L'(1/2, -1/2)\} \{\bar{\mathbf{m}}L(-1/2, 1/2) + \mathbf{m}L(1/2, -1/2)\}, \tag{A1f}
\end{aligned}$$

$$H_{23}^{\text{BLFQ}} = \frac{2G_\pi b^2}{\pi} [\bar{\mathbf{m}}L'(-1/2, 1/2) + \mathbf{m}L'(1/2, -1/2)][\bar{\mathbf{m}}L(-1/2, 1/2) + \mathbf{m}L(1/2, -1/2)], \tag{A1g}$$

$$\begin{aligned}
H_{24}^{\text{BLFQ}} = & \frac{2G_\pi b^3}{\pi} \bar{\mathbf{m}}\{\mathbf{m}[L'(-1/2, 3/2) + 2L'(-1/2, 1/2)]L(0, 0) - L'(-1/2, 1/2)L(0, 1)\} \\
& + \frac{2G_\pi b^3}{\pi} \mathbf{m}\{[L'(1/2, 1/2) + 2L'(1/2, -1/2)]L(0, 0) + L'(1/2, -1/2)L(0, 1)\}, \tag{A1h}
\end{aligned}$$

$$H_{31}^{\text{BLFQ}} = H_{13}^{\text{BLFQ}}, \tag{A1i}$$

$$H_{32}^{\text{BLFQ}} = H_{23}^{\text{BLFQ}}, \tag{A1j}$$

$$\begin{aligned}
H_{33}^{\text{BLFQ}} = & (\mathbf{m} + \bar{\mathbf{m}})^2 + 3\kappa^2 - \frac{G_\pi b^2}{\pi} \bar{\mathbf{m}}\mathbf{m} \{L'(1/2, 1/2)L(-1/2, -1/2) \\
& + L'(-1/2, 1/2)L(1/2, -1/2) + L'(1/2, -1/2)L(-1/2, 1/2) + L'(-1/2, -1/2)L(1/2, 1/2) \\
& + L'(-1/2, 3/2)L(-1/2, -1/2) - 2L'(-1/2, 1/2)L(-1/2, 1/2) + L'(-1/2, -1/2)L(-1/2, 3/2)\} \\
& - \frac{2G_\pi b^2}{\pi} [\bar{\mathbf{m}}L'(-1/2, 1/2) + \mathbf{m}L'(1/2, -1/2)][\bar{\mathbf{m}}L(-1/2, 1/2) + \mathbf{m}L(1/2, -1/2)], \tag{A1k}
\end{aligned}$$

$$H_{34}^{\text{BLFQ}} = -\frac{4G_\pi b^3}{\pi} \{\mathbf{m}[L'(1/2, -1/2)L(0, 1) + L'(1/2, -1/2)L(0, 0)] + \bar{\mathbf{m}}L'(-1/2, 1/2)L(0, 0)\}, \tag{A1l}$$

$$H_{41}^{\text{BLFQ}} = H_{14}^{\text{BLFQ}}, \tag{A1m}$$

$$H_{42}^{\text{BLFQ}} = H_{24}^{\text{BLFQ}}, \tag{A1n}$$

$$H_{43}^{\text{BLFQ}} = H_{34}^{\text{BLFQ}}, \tag{A1o}$$

$$H_{44}^{\text{BLFQ}} = (\mathbf{m} + \bar{\mathbf{m}})^2 + 5\kappa^2 - \frac{8G_\pi b^4}{\pi} L'(0, 0)L(0, 0). \tag{A1p}$$

The model parameters are specified in Table III.

APPENDIX B: ANALYTICAL EXPRESSIONS FOR INTEGRALS OF BASIS FUNCTIONS

1. Integrals for the calculation of the decay constant

When calculating the decay constants using the valence LFWFs of mesons, we encounter the following integral:

$$\begin{aligned}
\int_0^1 \frac{dx}{4\pi\sqrt{x(1-x)}} \int \frac{d^2\kappa^\perp}{(2\pi)^2} \phi_{nm} \left(\frac{\bar{\kappa}^\perp}{\sqrt{x(1-x)}} \right) \chi_l(x) &= \int_0^{2\pi} \frac{d\phi}{2\pi} e^{im\phi} \int_0^1 \frac{dx}{4\pi} \sqrt{x(1-x)} \chi_l(x) \int \frac{\rho d\rho}{2\pi b} \\
&\times \sqrt{\frac{4\pi n!}{(n+|m|)!}} \left(\frac{q}{b}\right)^{|m|} e^{-q^2/(2b^2)} L_n^{|m|}(q^2/b^2) q^{|m|} \\
&= \delta_{m,0} L_l(1/2, 1/2; \alpha, \beta) \frac{b}{\sqrt{\pi}} (-1)^n, \tag{B1}
\end{aligned}$$

where $L_l(1/2, 1/2; \alpha, \beta)$ is given by Eq. (B7). We have also used

$$\int_0^{+\infty} \frac{q dq}{2\pi b} \sqrt{4\pi} e^{-q^2/(2b^2)} L_n^0(q^2/b^2) = \frac{b}{\sqrt{\pi}} (-1)^n \tag{B2}$$

in deriving Eq. (B1).

2. Integrals for the mass radius

To evaluate the transverse integrals in Eq. (21), we first define $\vec{\rho} = b\sqrt{x(1-x)}\vec{r}^\perp$. After this substitution of variables we obtain

$$\begin{aligned} & \int_0^{+\infty} d|\vec{r}^\perp|^2 \int_0^{2\pi} \frac{d\phi_r}{2} x^2(1-x)^2 b^2 |\vec{r}^\perp|^2 \tilde{\phi}_{n',m'}^*(\sqrt{x(1-x)}\vec{r}^\perp) \tilde{\phi}_{n,m}(\sqrt{x(1-x)}\vec{r}^\perp) \\ &= b^{-2} \int_0^{+\infty} d\rho^2 \int_0^{2\pi} \frac{d\phi_r}{2} \rho^2 \tilde{\phi}_{n',m'}^*(\vec{\rho}^\perp/b) \tilde{\phi}_{n,m}(\vec{\rho}^\perp/b) \\ &= (-1)^{n'+n} \delta_{m'm} \sqrt{\frac{n'!n!}{(n'+|m|)!(n+|m|)!}} \int_0^{+\infty} d\rho^2 (\rho^2)^{|m|+1} e^{-\rho^2} L_{n'}^{|m|}(\rho^2) L_n^{|m|}(\rho^2). \end{aligned} \tag{B3}$$

The integrals over the product of generalized Laguerre polynomials can be obtained by the orthonormality relations. In order to apply such relations, we convert $L_n^{|m|}$ into $L_n^{|m|+1}$ using recurrence relations. From Eq. (22.7.30) of Ref. [101] we obtain

$$L_n^{|m|}(\rho^2) = L_n^{|m|+1}(\rho^2) - L_{n-1}^{|m|+1}(\rho^2). \tag{B4}$$

Here when $n = 0$, the second term drops out. We then have

$$\begin{aligned} & \sqrt{\frac{n'!n!}{(n'+|m|)!(n+|m|)!}} \int_0^{+\infty} d\rho^2 (\rho^2)^{|m|+1} e^{-\rho^2} L_{n'}^{|m|}(\rho^2) L_n^{|m|}(\rho^2) \\ &= \sqrt{\frac{n'!n!}{(n'+|m|)!(n+|m|)!}} \int_0^{+\infty} d\rho^2 (\rho^2)^{|m|+1} e^{-\rho^2} [L_{n'}^{|m|+1}(\rho^2) - \theta_{n'-1} L_{n'-1}^{|m|+1}(\rho^2)] [L_n^{|m|+1}(\rho^2) - \theta_{n-1} L_{n-1}^{|m|+1}(\rho^2)] \\ &= \sqrt{\frac{n'!n!}{(n'+|m|)!(n+|m|)!}} \left\{ \frac{(n+|m|+1)!}{n!} \delta_{n'n} - \frac{(n+|m|)!}{(n-1)!} \delta_{n',n-1} \theta_{n-1} - \frac{(n+|m|+1)!}{n!} \delta_{n',n+1} + \frac{(n+|m|)!}{(n-1)!} \delta_{n'n} \theta_{n-1} \right\} \\ &= (2n+|m|+1) \delta_{n'n} - \sqrt{n(n+|m|)} \delta_{n',n-1} - \sqrt{(n+1)(n+|m|+1)} \delta_{n',n+1} \end{aligned} \tag{B5}$$

with $n \in \mathbf{N}$ by default. Here $\theta_n = 1$ when $n \geq 0$ and $\theta_n = 0$ when $n < 0$.

The longitudinal integrals can be calculated by applying the orthonormal relation of the longitudinal basis function. Subsequently, we obtain the following expression for the Hermitian matrix that specifies the mass radius:

$$I_m(n', m', l'; n, m, l) = \delta_{l'l} \delta_{m'm} \{ (2n+|m|+1) \delta_{n'n} + \sqrt{n(n+|m|)} \delta_{n',n-1} + \sqrt{(n+1)(n+|m|+1)} \delta_{n',n+1} \}. \tag{B6}$$

3. Longitudinal integrals

Let us define the following integral in the longitudinal basis functions:

$$\begin{aligned} L_l(a, b; \alpha, \beta) &\equiv \int_0^1 \frac{dx}{4\pi} x^b (1-x)^a \chi_l(x; \alpha, \beta) \\ &= \sqrt{\frac{2l+\alpha+\beta+1}{4\pi}} \sqrt{\frac{\Gamma(l+1)\Gamma(l+\alpha+\beta+1)}{\Gamma(l+\alpha+1)\Gamma(l+\beta+1)}} \int_0^1 dx x^{\beta/2+b} (1-x)^{\alpha/2+a} P_l^{(\alpha,\beta)}(2x-1) \\ &= \sqrt{\frac{2l+\alpha+\beta+1}{4\pi}} \sqrt{\frac{\Gamma(l+1)\Gamma(l+\alpha+\beta+1)}{\Gamma(l+\alpha+1)\Gamma(l+\beta+1)}} \\ &\quad \times \sum_{m=0}^l \binom{l+\alpha}{m} \binom{l+\beta}{l-m} (-1)^{l-m} B\left(\frac{\beta}{2} + b + m + 1, \frac{\alpha}{2} + a + l - m + 1\right), \end{aligned} \tag{B7}$$

where $B(s, t) = \Gamma(s)\Gamma(t)/\Gamma(s+t)$ is the Euler beta function.

To evaluate $L_l(a, b; \alpha, \beta)$ numerically, we first rewrite Eq. (B7) as

$$L_l(a, b; \alpha, \beta) = \sqrt{\frac{2l+\alpha+\beta+1}{4\pi}} \sum_{m=0}^l C_{l,m}(a, b; \alpha, \beta), \tag{B8}$$

with

$$C_{l,m} \equiv \frac{(-1)^{l-m} \sqrt{\Gamma(l+1)\Gamma(l+\alpha+\beta+1)} \sqrt{\Gamma(l+\alpha+1)\Gamma(l+\beta+1)} \Gamma(\beta/2+b+m+1) \Gamma(\alpha/2+a+l-m+1)}{\Gamma(m+1)\Gamma(l+\alpha-m+1) \Gamma(l-m+1)\Gamma(\beta+m+1) \Gamma(\beta/2+b+\alpha/2+a+l+2)}. \tag{B9}$$

We then obtain the following recurrence relations for $C_{l,m}$:

$$C_{0,0} = \sqrt{\frac{\Gamma(\alpha + \beta + 1)}{\Gamma(\alpha + 1)\Gamma(\beta + 1)} \frac{\Gamma(\beta/2 + b + 1)\Gamma(\alpha/2 + a + 1)}{\Gamma(\beta/2 + b + \alpha/2 + a + 2)}}, \quad (\text{B10a})$$

$$\frac{C_{l,0}}{C_{l-1,0}} = -\sqrt{\frac{(l + \beta)(l + \alpha + \beta)}{l(l + \alpha)}} \frac{\alpha/2 + a + l}{\beta/2 + b + \alpha/2 + a + l + 1} \quad (\text{for } l \geq 1), \quad (\text{B10b})$$

$$\frac{C_{l,m}}{C_{l,m-1}} = -\frac{(l + \alpha - m + 1)(l - m + 1)}{m(\beta + m)(\alpha/2 + a + l - m + 1)} (\beta/2 + b + m) \quad (\text{for } l \geq m \geq 1). \quad (\text{B10c})$$

The longitudinal integral $L_l(a, b; \alpha, \beta)$ can then be calculated by first generating and then summing the following sequences:

$$\begin{array}{c} C_{0,0} \\ \downarrow \\ C_{1,0} + C_{1,1} \\ \downarrow \\ C_{2,0} + C_{2,1} + C_{2,2} \\ \downarrow \\ C_{3,0} + C_{3,1} + C_{3,2} + C_{3,3} \\ \downarrow \\ \dots \end{array}$$

using Eq. (B10).

APPENDIX C: ELECTROMAGNETIC FORM FACTORS IN THE BASIS REPRESENTATION

1. Reduction of the formula for the electromagnetic form factors in the valence Fock sector of mesons

Let us first expand the quark current operator in terms of creation and annihilation operators. In agreement with the light-front quantization condition, the Dirac field operator at a given light-front time $x^+ = 0$ is expanded according to

$$\psi(x) = \sum_{s=\pm 1/2} \int d\underline{p} [b_s(p)u_s(p)e^{-ip \cdot x} + d_s^\dagger(p)v_s(p)e^{ip \cdot x}]|_{x^+=0}, \quad (\text{C1})$$

where the flavor indices are implicit. Here $u_s(p)$ and $v_s(p)$ are solutions of the Dirac equation for free fermions. Meanwhile, the creation and annihilation operators satisfy these anticommutation relations:

$$\{b_r(k), b_s^\dagger(p)\} = \underline{\delta}(k - p)\delta_{rs}, \quad (\text{C2})$$

$$\{d_r(k), d_s^\dagger(p)\} = \underline{\delta}(k - p)\delta_{rs}, \quad (\text{C3})$$

while other anticommutation relations all vanish. We have defined the integral measure in the momentum space as

$$\int d\underline{p} = \int_0^{+\infty} \frac{dp^+}{4\pi p^+} \int_{-\infty}^{+\infty} \frac{dp_1^\perp}{2\pi} \int_{-\infty}^{+\infty} \frac{dp_2^\perp}{2\pi}. \quad (\text{C4})$$

The reduced delta function is defined according to

$$\underline{\delta}(k - p) = 4\pi k^+ \theta(k^+) \delta(k^+ - p^+) (2\pi)^2 \delta(\vec{k}^\perp - \vec{p}^\perp). \quad (\text{C5})$$

These conventions ensure that one reduced delta function can be utilized to eliminate one momentum-space integration.

With these definitions, the charge density operator becomes

$$\begin{aligned} \lim_{x \rightarrow 0} e_f \psi(x) \gamma^+ \psi(x) &= \lim_{x \rightarrow 0} \sum_{s's'} \int d\underline{p}' \int d\underline{p} [b_{s'}^\dagger(p') \bar{u}_{s'}(p') e^{ip' \cdot x} + d_{s'}(p') \bar{v}_{s'}(p') e^{-ip' \cdot x}] e_f \gamma^+ [b_s(p) u_s(p) e^{-ip \cdot x} + d_s^\dagger(p) v_s(p) e^{ip \cdot x}] \\ &\rightarrow \sum_{s's'} \int d\underline{p}' \int d\underline{p} \{e_q b_{s'}^\dagger(p') b_s(p) \bar{u}_{s'}(p') \gamma^+ u_s(p) - e_{\bar{q}} d_{s'}^\dagger(p') d_s(p) \bar{v}_{s'}(p') \gamma^+ v_s(p)\} \\ &= \sum_s \int d\underline{p}' \int d\underline{p} 2\sqrt{p'^+ p^+} [e_q b_s^\dagger(p') b_s(p) - e_{\bar{q}} d_s^\dagger(p') d_s(p)]. \end{aligned} \quad (\text{C6})$$

Here we have made use of $\bar{u}_{s'}(p')\gamma^+u_s(p) = 2\sqrt{p'^+p^+}\delta_{s's}$ and $\bar{v}_{s'}(p')\gamma^+v_s(p) = 2\sqrt{p'^+p^+}\delta_{s's}$. We have only kept terms of relevance to the valence Fock sector of mesons. The form factors then become

$$I_{m'_j, m_j}(Q^2) = \sum_{r's'} \int_0^1 \frac{dx'}{4\pi x'(1-x')} \int \frac{d\bar{k}'^\perp}{(2\pi)^2} \psi_{r's'}^*(x', \bar{k}'^\perp) \langle 0 | d_{s'}(k'_2) b_{r'}(k'_1) \sum_\sigma \int d\underline{p}' \int d\underline{p} \times \frac{\sqrt{p'^+p^+}}{P^+} [e_q b_\sigma^\dagger(p') b_\sigma(p) - e_{\bar{q}} d_\sigma^\dagger(p') d_\sigma(p)] \sum_{rs} \int_0^1 \frac{dx}{4\pi x(1-x)} \int \frac{d\bar{k}^\perp}{(2\pi)^2} b_r^\dagger(k_1) d_s^\dagger(k_2) | 0 \rangle \psi_{rs}(x, \bar{k}^\perp). \quad (C7)$$

The anticommutation relation for the creation and annihilation operator can be used to deduce

$$\sum_\sigma \int d\underline{p}' \int d\underline{p} d_{s'}(k'_2) b_{r'}(k'_1) b_\sigma^\dagger(p') b_\sigma(p) b_r^\dagger(k_1) d_s^\dagger(k) \sqrt{p'^+p^+} \rightarrow \sqrt{k_1'^+k_1^+} \delta_{r'r} \delta_{s's} \underline{\delta}(k'_2 - k_2), \quad (C8)$$

$$\sum_\sigma \int d\underline{p}' \int d\underline{p} d_{s'}(k'_2) b_{r'}(k'_1) d_\sigma^\dagger(p') d_\sigma(p) b_r^\dagger(k_1) d_s^\dagger(k) \sqrt{p'^+p^+} \rightarrow \sqrt{k_2'^+k_2^+} \delta_{r'r} \delta_{s's} \underline{\delta}(k'_1 - k_1). \quad (C9)$$

The expression for the form factors is then reduced to

$$I_{m'_j, m_j}(Q^2) = \sum_{rs} \int \frac{dx'}{4\pi x'(1-x')} \int \frac{d\bar{k}'^\perp}{(2\pi)^2} \psi_{rs}^*(x', \bar{k}'^\perp) \int \frac{dx}{4\pi x(1-x)} \int \frac{d\bar{k}^\perp}{(2\pi)^2} \psi_{rs}(x, \bar{k}^\perp) \times \left\{ e_q \frac{\sqrt{k_1'^+k_1^+}}{P^+} \underline{\delta}(k'_2 - k_2) - e_{\bar{q}} \frac{\sqrt{k_2'^+k_2^+}}{P^+} \underline{\delta}(k'_1 - k_1) \right\}, \quad (C10)$$

where we have defined

$$k_1^+ = xP^+, \quad (C11a)$$

$$\bar{k}_1^\perp = \bar{k}^\perp + x\bar{P}^\perp, \quad (C11b)$$

$$k_2^+ = (1-x)P^+, \quad (C11c)$$

$$\bar{k}_2^\perp = -\bar{k}^\perp + (1-x)\bar{P}^\perp,$$

and

$$k_1' = x'P'^+, \quad (C11d)$$

$$\bar{k}_1'^\perp = \bar{k}'^\perp + x'\bar{P}'^\perp, \quad (C11e)$$

$$k_2' = (1-x')P'^+, \quad (C11f)$$

$$\bar{k}_2'^\perp = -\bar{k}'^\perp + (1-x')\bar{P}'^\perp. \quad (C11g)$$

Meanwhile, the following reductions of delta functions hold in the Drell-Yan frame:

$$\underline{\delta}(k'_2 - k_2) = 4\pi(1-x)\delta(x' - x)(2\pi)^2\delta^2(-\bar{k}'^\perp + \bar{k}^\perp + (1-x)(\bar{P}'^\perp - \bar{P}^\perp)), \quad (C12)$$

$$\underline{\delta}(k'_1 - k_1) = 4\pi x\delta(x' - x)(2\pi)^2\delta^2(\bar{k}'^\perp - \bar{k}^\perp + x(\bar{P}'^\perp - \bar{P}^\perp)). \quad (C13)$$

Therefore, the expression for the form factors is reduced to that given on the right-hand side of Eq. (25) with $\bar{q}^\perp = \bar{P}'^\perp - \bar{P}^\perp$.

2. Electromagnetic form factors in the basis representation

In the basis representation, Eq. (25) becomes

$$I_{m'_j, m_j}(Q^2) = \sum_{n'm'l'} \sum_{nml} \sum_{rs} \psi_{n'm'l'rs}^* \psi_{nm lrs} \int \frac{dx}{4\pi x(1-x)} \chi_{l'}(x) \chi_l(x) \int \frac{d\vec{k}}{(2\pi)^2} \times \left\{ e_q \phi_{n'm'}^* \left(\frac{\bar{k}^\perp + (1-x)\bar{q}^\perp}{\sqrt{x(1-x)}} \right) - e_{\bar{q}} \phi_{n'm'}^* \left(\frac{\bar{k}^\perp - x\bar{q}^\perp}{\sqrt{x(1-x)}} \right) \right\} \phi_{nm}(x, \bar{k}^\perp) \\ = \sum_{n'm'l'} \sum_{nml} \sum_{rs} \psi_{n'm'l'rs}^* \psi_{nm lrs} \int \frac{dx}{4\pi x(1-x)} \chi_{l'}(x) \chi_l(x) \int \frac{d\vec{k}}{(2\pi)^2}$$

$$\times \left\{ e_q \phi_{n',-m'} \left(\frac{\vec{k}^\perp + (1-x)\vec{q}^\perp/2}{\sqrt{x(1-x)}} \right) \phi_{nm} \left(\frac{\vec{k}^\perp - (1-x)\vec{q}^\perp/2}{\sqrt{x(1-x)}} \right) - e_{\bar{q}} \phi_{n',-m'} \left(\frac{\vec{k}^\perp - x\vec{q}^\perp/2}{\sqrt{x(1-x)}} \right) \phi_{nm} \left(\frac{\vec{k}^\perp + x\vec{q}^\perp/2}{\sqrt{x(1-x)}} \right) \right\}, \quad (\text{C14})$$

where we have applied shifts in the transverse momentum and $\phi_{nm}^* = \phi_{n,-m}$.

We then apply the Talmi-Moshinsky (TM) transform to simplify the integrals in the transverse momentum [62,102]. Specifically, we have

$$\phi_{n',-m'}(\vec{q}_1) \phi_{n,m}(\vec{q}_2) = \sum_{NM\bar{n}\bar{m}} C(n', -m', n, m; N, M, \bar{n}, \bar{m}) \phi_{NM}(\vec{P}) \phi_{\bar{n}\bar{m}}(\vec{p}), \quad (\text{C15})$$

with all four harmonic oscillator functions sharing the same scale b and

$$\vec{P} = (\vec{q}_1 + \vec{q}_2)/\sqrt{2}, \quad \vec{p} = (\vec{q}_1 - \vec{q}_2)/\sqrt{2}, \quad (\text{C16})$$

which corresponds to

$$\vec{P} = \frac{\sqrt{2}\vec{k}^\perp}{\sqrt{x(1-x)}}, \quad \vec{p} = \sqrt{\frac{1-x}{2x}}\vec{q}^\perp \quad (\text{C17})$$

for the quark contribution and

$$\vec{P} = \frac{\sqrt{2}\vec{k}^\perp}{\sqrt{x(1-x)}}, \quad \vec{p} = -\sqrt{\frac{x}{2(1-x)}}\vec{q}^\perp \quad (\text{C18})$$

for the antiquark contribution.

The coefficient $C(n', -m', n, m; N, M, \bar{n}, \bar{m})$ can be computed with established procedures [62,102]. The following observations made specifically for the valence Fock sector of mesons will be helpful in enumerating terms after in the TM transform.

(i) Because the TM transform cannot change the total magnetic projection of the orbital angular momentum, we must have $-m' + m = M + \bar{m}$.

(ii) The integral in \vec{k}^\perp will select the terms with $\bar{m} = 0$, leaving other values of m not contributing to the integral.

(iii) Because the mesons obtained from the light-front Hamiltonian have fixed magnetic projection for the sum of the spin and orbital angular momenta, when the spins of the two wave functions in a bilinear are identical, so are their magnetic quantum numbers m' and m .

These observations further confine us to $\bar{m} = -m' + m = 0$, which is expected since the electromagnetic form factors have no angular dependence.

The integrals over the momenta of the light-front wave functions then become

$$\begin{aligned} \tilde{C}(n', m', l'; n, m, l; Q^2) &\equiv \int \frac{dx}{4\pi x(1-x)} \chi_{l'}(x) \chi_l(x) \int \frac{d\vec{k}^\perp}{(2\pi)^2} \left\{ e_q \phi_{n',-m'} \left(\frac{\vec{k}^\perp + (1-x)\vec{q}^\perp/2}{\sqrt{x(1-x)}} \right) \phi_{nm} \left(\frac{\vec{k}^\perp - (1-x)\vec{q}^\perp/2}{\sqrt{x(1-x)}} \right) \right. \\ &\quad \left. - e_{\bar{q}} \phi_{n',-m'} \left(\frac{\vec{k}^\perp - x\vec{q}^\perp/2}{\sqrt{x(1-x)}} \right) \phi_{nm} \left(\frac{\vec{k}^\perp + x\vec{q}^\perp/2}{\sqrt{x(1-x)}} \right) \right\} \\ &= \int \frac{dx}{4\pi x(1-x)} \chi_{l'}(x) \chi_l(x) \sum_{NM\bar{n}\bar{m}} C(n', -m', n, m; N, M, \bar{n}, \bar{m}) \int \frac{d\vec{k}}{(2\pi)^2} \phi_{NM} \left(\frac{\sqrt{2}\vec{k}^\perp}{\sqrt{x(1-x)}} \right) \\ &\quad \times \left\{ e_q \phi_{\bar{n}\bar{m}} \left(\sqrt{\frac{1-x}{2x}}\vec{q}^\perp \right) - e_{\bar{q}} \phi_{\bar{n}\bar{m}} \left(-\sqrt{\frac{x}{2(1-x)}}\vec{q}^\perp \right) \right\} \\ &= \int \frac{dx}{4\pi} \chi_{l'}(x) \chi_l(x) \sum_{NM\bar{n}\bar{m}} \frac{(-1)^N b}{2\sqrt{\pi}} \delta_{M0} C(n', -m', n, m; N, M, \bar{n}, \bar{m}) \left\{ e_q \phi_{\bar{n}\bar{m}} \left(\sqrt{\frac{1-x}{2x}}\vec{q}^\perp \right) \right. \\ &\quad \left. - e_{\bar{q}} \phi_{\bar{n}\bar{m}} \left(-\sqrt{\frac{x}{2(1-x)}}\vec{q}^\perp \right) \right\} \\ &= \delta_{n'm} \sum_{N\bar{n}} C(n', -m', n, m; N, 0, \bar{n}, 0) \int \frac{dx}{4\pi} \chi_{l'}(x) \chi_l(x) \frac{(-1)^N b}{2\sqrt{\pi}} \\ &\quad \times \left\{ e_q \phi_{\bar{n}0} \left(\sqrt{\frac{1-x}{2x}}\vec{q}^\perp \right) - e_{\bar{q}} \phi_{\bar{n}0} \left(-\sqrt{\frac{x}{2(1-x)}}\vec{q}^\perp \right) \right\} \end{aligned}$$

$$\begin{aligned}
&= \delta_{m'm} \sum_{N\bar{n}} C(n', -m', n, m; N, 0, \bar{n}, 0) \int \frac{dx}{4\pi} \chi_{l'}(x) \chi_l(x) (-1)^N \\
&\quad \times \left\{ e_q \exp\left(-\frac{1-x}{2x} \frac{Q^2}{2b^2}\right) L_{\bar{n}}\left(\frac{1-x}{2x} \frac{Q^2}{b^2}\right) - e_{\bar{q}} \exp\left(-\frac{x}{2(1-x)} \frac{Q^2}{2b^2}\right) L_{\bar{n}}\left(\frac{x}{2(1-x)} \frac{Q^2}{b^2}\right) \right\}.
\end{aligned} \tag{C19}$$

With the aid of the TM transform, the electromagnetic form factors in the basis representation become

$$I_{m'_j, m_j}(Q^2) = \sum_{n'm'l'} \sum_{n,m,l} \sum_{r,s} \psi_{n'm'l'rs}^* \tilde{C}(n', m', l'; n, m, l; Q^2) \psi_{nmrlrs}. \tag{C20}$$

APPENDIX D: MULTIQUBIT OBSERVABLES FOR THE $J_z = 0$ SECTOR OF THE $N_{\max} = L_{\max} = 0, M_{\max} = 2$ HAMILTONIAN

Following, we provide the multiqubit expressions for observables discussed in Sec. III for the $J_z = 0$ sector of the BLFQ pion Hamiltonian. The decay constant can be obtained from Eq. (16) as

$$\begin{aligned}
f_\pi &= 61.6 |\langle v | \psi(\vec{\theta}) \rangle|, \\
|v\rangle &= (0, 1/\sqrt{2}, -1/\sqrt{2}, 0).
\end{aligned} \tag{D1}$$

In order to reduce the gate count, rather than using the circuit from Fig. 2, we expand the projector onto the $|v\rangle$ state in terms of Pauli operators:

$$|v\rangle\langle v| = \frac{1}{2} \begin{pmatrix} 0 & 0 & 0 & 0 \\ 0 & 1 & -1 & 0 \\ 0 & -1 & 1 & 0 \\ 0 & 0 & 0 & 0 \end{pmatrix}, \tag{D2}$$

$$|v\rangle\langle v|_{\text{direct}} = 0.5IIII - 0.25(IXXI + IYYI + IZII + IIZI), \tag{D3}$$

$$|v\rangle\langle v|_{\text{compact}} = 0.25(II - XX - YY - ZZ) \tag{D4}$$

and calculate the decay constant using $|\langle v | \psi(\vec{\theta}) \rangle| = \sqrt{\langle \psi(\vec{\theta}) | (|v\rangle\langle v|) | \psi(\vec{\theta}) \rangle}$.

The mass radius matrix is given by Eq. (22), which when expressed in terms of qubit operators, is

$$\frac{3}{2b^2} I_m = \begin{pmatrix} 2.27 & 0 & 0 & 0 \\ 0 & 1.13 & 0 & 0 \\ 0 & 0 & 1.13 & 0 \\ 0 & 0 & 0 & 2.27 \end{pmatrix}, \tag{D5}$$

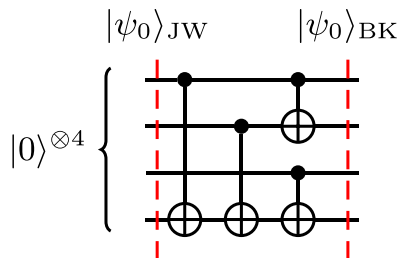


FIG. 9. Converting a four-qubit state from Jordan-Wigner to Bravyi-Kitaev encoding.

$$\begin{aligned}
\frac{3}{2b^2} I_{m, \text{direct}} &= -1.30(IIIZ + ZIII) - 0.65(IIZI + IZII) \\
&\quad + 3.92IIII,
\end{aligned} \tag{D6}$$

$$\frac{3}{2b^2} I_{m, \text{compact}} = 1.96II + 0.65ZZ. \tag{D7}$$

The $\rho_{l=0, l'=0}$ density matrix of the parton distribution function is given by Eqs. (23)–(24b), which when expressed in terms of qubit operators is

$$\rho = \begin{pmatrix} 1 & 0 & 0 & 0 \\ 0 & 1 & 0 & 0 \\ 0 & 0 & 1 & 0 \\ 0 & 0 & 0 & 1 \end{pmatrix}, \tag{D8}$$

$$\rho_{\text{direct}} = 2IIII - 0.5(ZIII + IZII + IIZI + IIIZ), \tag{D9}$$

$$\rho_{\text{compact}} = II. \tag{D10}$$

We calculate the elastic form-factor matrix $F_P(Q^2)$ [Eq. (27)] by discretizing Q^2 on the interval $0 \leq Q^2 \leq 5152900$, evaluating the matrix $\tilde{C}(n', m', l'; n, m, l; Q^2)$ for each value of Q^2 , and expanding it in terms of Pauli operators. For the sake of brevity, we do not include these explicit expressions for each point.

APPENDIX E: BRAVYI-KITAEV ENCODING

Both Jordan-Wigner and Bravyi-Kitaev encoding allow one to store the second-quantized fermionic states in a quantum computer. Within the Jordan-Wigner encoding, each qubit stores the occupancy of a particular orbital [75]. Within the Bravyi-Kitaev encoding, the information about parity is distributed equally between the operators and states [76]. In practice, one typically uses the more efficient BK encoding. While a single fermionic orbital in BK encoding is represented by up to $O(\log N)$ qubits [instead of $O(N)$ in JW], the creation and annihilation operators are represented now by $\log N$ -local multiqubit operators [76].

The BK-encoded basis states $|\dots b_2 b_1 b_0\rangle$ can be obtained from the JW-encoded states by means of the linear transformation $b_i = \sum_{ij} \mathcal{P}_{ij} f_j$ [78], where the entries of \mathcal{P}_{ij} are $\{0, 1\}$, and multiplication modulo 2 is implied. Such a transformation of states can be implemented efficiently on a quantum computer. Since the matrix \mathcal{P}_{ij} is lower triangular [78], multiplication modulo 2 can be performed on qubits using the controlled-NOT (CNOT) gates, starting from the *bottom* row. For example, in the case of four qubits, the encoded matrix

has the form of

$$\mathcal{P}_{ij} = \begin{pmatrix} 1 & 0 & 0 & 0 \\ 1 & 1 & 0 & 0 \\ 0 & 0 & 1 & 0 \\ 1 & 1 & 1 & 1 \end{pmatrix}. \quad (\text{E1})$$

The corresponding circuit is shown on Fig. 9.

In order to perform the simulation in the BK encoding, one adjusts the procedure outlined in Sec. IV A as follows: (a) After preparing the JW-encoded initial state $|\psi_0\rangle$, one appends to the circuit a block converting JW-encoded states to BK-encoded ones as on Fig. 9; (b) Eq. (34) is replaced with its BK version which changes the coefficients α_j in (35) and h_i in Eq. (37).

-
- [1] R. P. Feynman, Simulating physics with computers, *Int. J. Theor. Phys.* **21**, 467 (1982).
- [2] S. P. Jordan, K. S. M. Lee, and J. Preskill, Quantum algorithms for quantum field theories, *Science* **336**, 1130 (2012).
- [3] S. Lloyd, Universal quantum simulators, *Science* **273**, 1073 (1996).
- [4] C. Zalka, Simulating quantum systems on a quantum computer, *Proc. R. Soc. London A* **454**, 313 (1998).
- [5] S. Wiesner, Simulations of many-body quantum systems by a quantum computer, [arXiv:quant-ph/9603028](https://arxiv.org/abs/quant-ph/9603028).
- [6] B. M. Boghosian and W. Taylor, Quantum lattice-gas models for the many-body schrödinger equation, *Int. J. Mod. Phys. C* **8**, 705 (1997).
- [7] D. A. Meyer, From quantum cellular automata to quantum lattice gases, *J. Stat. Phys.* **85**, 551 (1996).
- [8] A. Aspuru-Guzik, A. D. Dutoi, P. J. Love, and M. Head-Gordon, Simulated quantum computation of molecular energies, *Science* **309**, 1704 (2005).
- [9] L.-A. Wu, M. S. Byrd, and D. A. Lidar, Polynomial-Time Simulation of Pairing Models on a Quantum Computer, *Phys. Rev. Lett.* **89**, 057904 (2002).
- [10] D. W. Berry, A. M. Childs, R. Cleve, R. Kothari, and R. D. Somma, Exponential improvement in precision for simulating sparse Hamiltonians, in *Proceedings of the 46th Annual Symposium on Theory of Computing* (ACM, New York, 2014), pp. 283–292.
- [11] G. H. Low and I. L. Chuang, Optimal Hamiltonian Simulation by Quantum Signal Processing, *Phys. Rev. Lett.* **118**, 010501 (2017).
- [12] G. H. Low and I. L. Chuang, Hamiltonian simulation by qubitization, *Quantum* **3**, 163 (2019).
- [13] D. W. Berry, A. M. Childs, and R. Kothari, Hamiltonian simulation with nearly optimal dependence on all parameters, in *2015 IEEE 56th Annual Symposium on Foundations of Computer Science* (IEEE, Piscataway, NJ, 2015), pp. 792–809.
- [14] D. W. Berry, A. M. Childs, R. Cleve, R. Kothari, and R. D. Somma, Simulating Hamiltonian Dynamics with a Truncated Taylor Series, *Phys. Rev. Lett.* **114**, 090502 (2015).
- [15] A. Peruzzo, J. McClean, P. Shadbolt, M.-H. Yung, X.-Q. Zhou, P. J. Love, A. Aspuru-Guzik, and J. L. O’Brien, A variational eigenvalue solver on a photonic quantum processor, *Nat. Commun.* **5**, 4213 (2014).
- [16] J. R. McClean, J. Romero, R. Babbush, and A. Aspuru-Guzik, The theory of variational hybrid quantum-classical algorithms, *New J. Phys.* **18**, 023023 (2016).
- [17] N. Moll, P. Barkoutsos, L. S. Bishop, J. M. Chow, A. Cross, D. J. Egger, S. Filipp, A. Fuhrer, J. M. Gambetta, M. Ganzhorn *et al.*, Quantum optimization using variational algorithms on near-term quantum devices, *Quantum Sci. Technol.* **3**, 030503 (2018).
- [18] M. Cerezo, A. Arrasmith, R. Babbush, S. C. Benjamin, S. Endo, K. Fujii, J. R. McClean, K. Mitarai, X. Yuan, L. Cincio, and P. J. Coles, Variational quantum algorithms, [arXiv:2012.09265](https://arxiv.org/abs/2012.09265).
- [19] A. H. Moosavian and S. Jordan, Faster quantum algorithm to simulate fermionic quantum field theory, *Phys. Rev. A* **98**, 012332 (2018).
- [20] S. P. Jordan, H. Krovi, K. S. M. Lee, and J. Preskill, BQP-completeness of scattering in scalar quantum field theory, *Quantum* **2**, 44 (2018).
- [21] X. Zhang, K. Zhang, Y. Shen, S. Zhang, J.-N. Zhang, M.-H. Yung, J. Casanova, J. S. Pedernales, L. Lamata, E. Solano, and K. Kim, Experimental quantum simulation of fermion-antifermion scattering via boson exchange in a trapped ion, *Nat. Commun.* **9**, 195 (2018).
- [22] U.-J. Wiese, Towards quantum simulating QCD, *Nucl. Phys. A* **931**, 246 (2014).
- [23] E. Zohar, J. I. Cirac, and B. Reznik, Quantum simulations of lattice gauge theories using ultracold atoms in optical lattices, *Rep. Prog. Phys.* **79**, 014401 (2015).
- [24] E. Zohar, J. I. Cirac, and B. Reznik, Cold-atom Quantum Simulator for su(2) Yang-Mills Lattice Gauge Theory, *Phys. Rev. Lett.* **110**, 125304 (2013).
- [25] E. Zohar, J. I. Cirac, and B. Reznik, Quantum simulations of gauge theories with ultracold atoms: Local gauge invariance from angular-momentum conservation, *Phys. Rev. A* **88**, 023617 (2013).
- [26] D. González-Cuadra, E. Zohar, and J. I. Cirac, Quantum simulation of the Abelian-Higgs lattice gauge theory with ultracold atoms, *New J. Phys.* **19**, 063038 (2017).
- [27] S. Barrett, K. Hammerer, S. Harrison, T. E. Northup, and T. J. Osborne, Simulating Quantum Fields with Cavity QED, *Phys. Rev. Lett.* **110**, 090501 (2013).
- [28] K. Marshall, R. Pooser, G. Siopsis, and C. Weedbrook, Quantum simulation of quantum field theory using continuous variables, *Phys. Rev. A* **92**, 063825 (2015).
- [29] C. W. Bauer, W. A. De Jong, B. Nachman, and D. Provasoli, A Quantum Algorithm for High Energy Physics Simulations, *Phys. Rev. Lett.* **126**, 062001 (2021).
- [30] E. A. Martinez, C. A. Muschik, P. Schindler, D. Nigg, A. Erhard, M. Heyl, P. Hauke, M. Dalmonte, T. Monz, P. Zoller *et al.*, Real-time dynamics of lattice gauge theories with a few-qubit quantum computer, *Nature (London)* **534**, 516 (2016).
- [31] C. Muschik, M. Heyl, E. Martinez, T. Monz, P. Schindler, B. Vogell, M. Dalmonte, P. Hauke, R. Blatt, and P. Zoller, U(1)

- Wilson lattice gauge theories in digital quantum simulators, *New J. Phys.* **19**, 103020 (2017).
- [32] N. Klco, E. F. Dumitrescu, A. J. McCaskey, T. D. Morris, R. C. Pooser, M. Sanz, E. Solano, P. Lougovski, and M. J. Savage, Quantum-classical computation of schwinger model dynamics using quantum computers, *Phys. Rev. A* **98**, 032331 (2018).
- [33] N. Klco and M. J. Savage, Digitization of scalar fields for quantum computing, *Phys. Rev. A* **99**, 052335 (2019).
- [34] N. Mueller, A. Tarasov, and R. Venugopalan, Deeply inelastic scattering structure functions on a hybrid quantum computer, *Phys. Rev. D* **102**, 016007 (2020).
- [35] J. Liu and Y. Xin, Quantum simulation of quantum field theories as quantum chemistry, *J. High Energy Phys.* **12** (2020) 011.
- [36] S. P. Jordan, K. S. M. Lee, and J. Preskill, Quantum algorithms for fermionic quantum field theories, [arXiv:1404.7115](https://arxiv.org/abs/1404.7115).
- [37] H. Lamm, S. Lawrence, and Y. Yamauchi, Parton physics on a quantum computer, *Phys. Rev. Research* **2**, 013272 (2020).
- [38] T. Farrelly and J. Streich, Discretizing quantum field theories for quantum simulation, [arXiv:2002.02643](https://arxiv.org/abs/2002.02643).
- [39] C. Gidney and M. Ekerå, How to factor 2048 bit rsa integers in 8 hours using 20 million noisy qubits, *Quantum* **5**, 433 (2021).
- [40] M. G. Whitney, N. Isailovic, Y. Patel, and J. Kubiawicz, A fault tolerant, area efficient architecture for Shor's factoring algorithm, in *Proceedings of the 36th Annual International Symposium on Computer Architecture* (ACM, New York, 2009), pp. 383–394.
- [41] M. Kreshchuk, W. M. Kirby, G. Goldstein, H. Beauchemin, and P. J. Love, Quantum Simulation of Quantum Field Theory in the Light-Front Formulation, [arXiv:2002.04016](https://arxiv.org/abs/2002.04016).
- [42] M. Kreshchuk, S. Jia, W. M. Kirby, G. Goldstein, J. P. Vary, and P. J. Love, Light-front field theory on current quantum computers, *Entropy* **23**, 597 (2021).
- [43] J. P. Vary, H. Honkanen, J. Li, P. Maris, S. J. Brodsky, A. Harindranath, G. F. de Teramond, P. Sternberg, E. G. Ng, and C. Yang, Hamiltonian light-front field theory in a basis function approach, *Phys. Rev. C* **81**, 035205 (2010).
- [44] X. Zhao, Advances in Basis Light-front Quantization, *Few-Body Syst.* **56**, 257 (2015).
- [45] Y. Li, P. Maris, X. Zhao, and J. P. Vary, Heavy quarkonium in a holographic basis, *Phys. Lett. B* **758**, 118 (2016).
- [46] Y. Li, P. Maris, and J. P. Vary, Quarkonium as a relativistic bound state on the light front, *Phys. Rev. D* **96**, 016022 (2017).
- [47] S. Tang, Y. Li, P. Maris, and J. P. Vary, B_c mesons and their properties on the light front, *Phys. Rev. D* **98**, 114038 (2018).
- [48] S. Tang, Y. Li, P. Maris, and J. P. Vary, Heavy-light mesons on the light front, *Eur. Phys. J. C* **80**, 522 (2020).
- [49] J. Lan, C. Mondal, S. Jia, X. Zhao, and J. P. Vary, Parton Distribution Functions from a Light Front Hamiltonian and QCD Evolution for Light Mesons, *Phys. Rev. Lett.* **122**, 172001 (2019).
- [50] J. Lan, C. Mondal, M. Li, Y. Li, S. Tang, X. Zhao, and J. P. Vary, Parton distribution functions of heavy mesons on the light front, *Phys. Rev. D* **102**, 014020 (2020).
- [51] J. Lan, C. Mondal, S. Jia, X. Zhao, and J. P. Vary, Pion and kaon parton distribution functions from basis light front quantization and QCD evolution, *Phys. Rev. D* **101**, 034024 (2020).
- [52] S. Jia and J. P. Vary, Basis light front quantization for the charged light mesons with color singlet Nambu–Jona-Lasinio interactions, *Phys. Rev. C* **99**, 035206 (2019).
- [53] S. P. Klevansky, The Nambu–Jona-Lasinio model of quantum chromodynamics, *Rev. Mod. Phys.* **64**, 649 (1992).
- [54] V. V. Shende, S. S. Bullock, and I. L. Markov, Synthesis of quantum-logic circuits, *IEEE Trans. Computer-Aided Design Integrat. Circ. Syst.* **25**, 1000 (2006).
- [55] D. Cruz, R. Fournier, F. Gremion, A. Jeannerot, K. Komagata, T. Tomic, J. Thiesbrummel, C. L. Chan, N. Macris, M.-A. Dupertuis, and C. Javerzac-Galy, Efficient quantum algorithms for ghz and w states, and implementation on the IBM quantum computer, *Adv. Quantum Technol.* **2**, 1900015 (2019).
- [56] X. Zhao, K. Fu, H. Zhao, J. Lan, C. Mondal, S. Xu, and J. P. Vary, Recent progress in basis light-front quantization, in *18th International Conference on Hadron Spectroscopy and Structure* (World Scientific, Singapore, 2020), p. 4.
- [57] S. J. Brodsky, H.-C. Pauli, and S. S. Pinsky, Quantum chromodynamics and other field theories on the light cone, *Phys. Rep.* **301**, 299 (1998).
- [58] J. P. Vary, L. Adhikari, G. Chen, M. Li, Y. Li, P. Maris, W. Qian, J. R. Spence, S. Tang, K. Tuchin, and X. Zh, Trends and Progress in Nuclear and Hadron Physics: A straight or winding road, *Few-Body Syst.* **58**, 56 (2017).
- [59] U. Vogl, M. F. M. Lutz, S. Klimt, and W. Weise, Generalized SU(3) Nambu–Jona-Lasinio model. Part 2. From current to constituent quarks, *Nucl. Phys.* **A516**, 469 (1990).
- [60] U. Vogl and W. Weise, The Nambu and Jona Lasinio model: Its implications for hadrons and nuclei, *Prog. Part. Nucl. Phys.* **27**, 195 (1991).
- [61] S. Klimt, M. F. M. Lutz, U. Vogl, and W. Weise, Generalized SU(3) Nambu–Jona-Lasinio model. Part 1. Mesonic modes, *Nucl. Phys.* **A516**, 429 (1990).
- [62] P. Wiecki, Y. Li, X. Zhao, P. Maris, and J. P. Vary, Basis light-front quantization approach to positronium, *Phys. Rev. D* **91**, 105009 (2015).
- [63] S. D. Drell and T.-M. Yan, Connection of Elastic Electromagnetic Nucleon form Factors at Large Q^2 and Deep Inelastic Structure Functions Near Threshold, *Phys. Rev. Lett.* **24**, 181 (1970).
- [64] G. B. West, Phenomenological Model for the Electromagnetic Structure of the Proton, *Phys. Rev. Lett.* **24**, 1206 (1970).
- [65] S. P. Jordan, K. S. M. Lee, and J. Preskill, Quantum computation of scattering in scalar quantum field theories, *Quantum Inf. Comput.* **14**, 1014 (2014).
- [66] J. Romero, R. Babbush, J. R. McClean, C. Hempel, P. J. Love, and A. Aspuru-Guzik, Strategies for quantum computing molecular energies using the unitary coupled cluster Ansatz, *Quantum Sci. Technol.* **4**, 014008 (2018).
- [67] I. C. Cloët, M. R. Dietrich, J. Arrington, A. Bazavov, M. Bishof, A. Freese, A. V. Gorshkov, A. Grassellino, K. Hafidi, Z. Jacob *et al.*, Opportunities for nuclear physics and quantum information science, [arXiv:1903.05453](https://arxiv.org/abs/1903.05453).
- [68] J. R. McClean, S. Boixo, V. N. Smelyanskiy, R. Babbush, and H. Neven, Barren plateaus in quantum neural network training landscapes, *Nat. Commun.* **9**, 4812 (2018).
- [69] A. Uvarov and J. Biamonte, On barren plateaus and cost function locality in variational quantum algorithms, *J. Phys. A: Math. Theor.* **54** 245301 (2021).

- [70] M. Cerezo, A. Sone, T. Volkoff, L. Cincio, and P. J. Coles, Cost function dependent barren plateaus in shallow parametrized quantum circuits, *Nat. Commun.* **12**, 1791 (2021).
- [71] S. Wang, E. Fontana, M. Cerezo, K. Sharma, A. Sone, L. Cincio, and P. J. Coles, Noise-induced barren plateaus in variational quantum algorithms, [arXiv:2007.14384](https://arxiv.org/abs/2007.14384).
- [72] S. McArdle, T. Jones, S. Endo, Y. Li, S. C. Benjamin, and X. Yuan, Variational ansatz-based quantum simulation of imaginary time evolution, *npj Quantum Inf.* **5**, 75 (2019).
- [73] M. Motta, C. Sun, A. T. K. Tan, M. J. O'Rourke, E. Ye, A. J. Minnich, F. G. S. L. Brandão, and G. K.-L. Chan, Determining eigenstates and thermal states on a quantum computer using quantum imaginary time evolution, *Nat. Phys.* **16**, 205 (2020).
- [74] R. Somma, G. Ortiz, J. E. Gubernatis, E. Knill, and R. Laflamme, Simulating physical phenomena by quantum networks, *Phys. Rev. A* **65**, 042323 (2002).
- [75] P. Jordan and E. Wigner, Über das paulische äquivalenzverbot, *Z. Phys.* **47**, 631 (1928).
- [76] S. B. Bravyi and A. Y. Kitaev, Fermionic quantum computation, *Ann. Phys.* **298**, 210 (2002).
- [77] J. T. Seeley, M. J. Richard, and P. J. Love, The Bravyi-Kitaev transformation for quantum computation of electronic structure, *J. Chem. Phys.* **137**, 224109 (2012).
- [78] A. Tranter, S. Sofia, J. Seeley, M. Kaicher, J. McClean, R. Babbush, P. V. Coveney, F. Mintert, F. Wilhelm, and P. J. Love, The Bravyi-Kitaev transformation: Properties and applications, *Int. J. Quantum Chem.* **115**, 1431 (2015).
- [79] K. Setia and J. D. Whitfield, Bravyi-Kitaev superfast simulation of electronic structure on a quantum computer, *J. Chem. Phys.* **148**, 164104 (2018).
- [80] R. Babbush, D. W. Berry, I. D. Kivlichan, A. Y. Wei, P. J. Love, and A. Aspuru-Guzik, Exponentially more precise quantum simulation of fermions in second quantization, *New J. Phys.* **18**, 033032 (2016).
- [81] B. Toloui and P. J. Love, Quantum algorithms for quantum chemistry based on the sparsity of the CI-matrix, [arXiv:1312.2579](https://arxiv.org/abs/1312.2579).
- [82] Google AI Quantum and Collaborators, Hartree-Fock on a superconducting qubit quantum computer, *Science* **369**, 1084 (2020).
- [83] H. Honkanen, P. Maris, J. P. Vary, and S. J. Brodsky, Electron in a Transverse Harmonic Cavity, *Phys. Rev. Lett.* **106**, 061603 (2011).
- [84] X. Zhao, H. Honkanen, P. Maris, J. P. Vary, and S. J. Brodsky, Electron g-2 in Light-Front Quantization, *Phys. Lett. B* **737**, 65 (2014).
- [85] X. Zhao, K. Fu, H. Zhao, and J. Vary, Positronium: An illustration of nonperturbative renormalization in a basis light-front approach, *Proc. Sci.* **374**, 090 (2020).
- [86] Z. Hu, S. Xu, C. Mondal, X. Zhao, and J. P. Vary, Transverse structure of electron in momentum space in basis light-front quantization, *Phys. Rev. D* **103**, 036005 (2021).
- [87] O. Christiansen, Vibrational coupled cluster theory, *J. Chem. Phys.* **120**, 2149 (2004).
- [88] S. McArdle, A. Mayorov, X. Shan, S. Benjamin, and X. Yuan, Digital quantum simulation of molecular vibrations, *Chem. Sci.* **10**, 5725 (2019).
- [89] P. J. Ollitrault, A. Baiardi, M. Reiher, and I. Tavernelli, Hardware efficient quantum algorithms for vibrational structure calculations, *Chem. Sci.* **11**, 6842 (2020).
- [90] R. D. Somma, Quantum computation, complexity, and many-body physics, [arXiv:quant-ph/0512209](https://arxiv.org/abs/quant-ph/0512209).
- [91] A. Macridin, P. Spentzouris, J. Amundson, and R. Harnik, Electron-Phonon Systems on a Universal Quantum Computer, *Phys. Rev. Lett.* **121**, 110504 (2018).
- [92] N. P. D. Sawaya and J. Huh, Quantum algorithm for calculating molecular vibronic spectra, *J. Phys. Chem. Lett.* **10**, 3586 (2019).
- [93] D. Wecker, M. B. Hastings, and M. Troyer, Progress towards practical quantum variational algorithms, *Phys. Rev. A* **92**, 042303 (2015).
- [94] A. Zhao, A. Tranter, W. M. Kirby, S. F. Ung, A. Miyake, and P. J. Love, Measurement reduction in variational quantum algorithms, *Phys. Rev. A* **101**, 062322 (2020).
- [95] P. Gokhale, O. Angiuli, Y. Ding, K. Gui, T. Tomesh, M. Suchara, M. Martonosi, and F. T. Chong, $\mathcal{O}(n^3)$ measurement cost for variational quantum eigensolver on molecular Hamiltonians, *IEEE Trans. Quantum Eng.* **1**, 1 (2020).
- [96] W. M. Kirby and P. J. Love, Variational quantum eigensolvers for sparse Hamiltonians, [arXiv:2012.07171](https://arxiv.org/abs/2012.07171).
- [97] G. Aleksandrowicz, T. Alexander, P. Barkoutsos, L. Bello, Y. Ben-Haim, D. Bucher, F. J. Cabrera-Hernández, J. Carballo-Franquis, A. Chen, C.-F. Chen *et al.*, QISKIT: An open-source framework for quantum computing, *Zenodo* (2019), doi: [10.5281/zenodo.2562111](https://doi.org/10.5281/zenodo.2562111).
- [98] R. H. Byrd, P. Lu, J. Nocedal, and C. Zhu, A limited memory algorithm for bound constrained optimization, *SIAM J. Sci. Comput.* **16**, 1190 (1995).
- [99] M. J. Powell, A direct search optimization method that models the objective and constraint functions by linear interpolation, in *Advances in Optimization and Numerical Analysis*, edited by S. Gomez and J. P. Hennart (Kluwer, Dordrecht, 1994), pp. 51–67.
- [100] S. J. Brodsky and G. F. de Teramond, Light-Front Holography and AdS/QCD Correspondence, QCD Downunder II Auckland, Auckland, New Zealand, January 17-19, 2008 (unpublished).
- [101] M. Abramowitz and I. A. Stegun, *Handbook of Mathematical Functions: With Formulas, Graphs, and Mathematical Tables*, Applied Mathematics Series (Dover, New York, 1964).
- [102] L. Chaos-Cador and E. Ley-Koo, Common generating functions of complete harmonic oscillator wave functions and transformation brackets in d dimensions, *Int. J. Quantum Chem.* **97**, 844 (2004).